

UNIVERSITÄT TÜBINGEN

MASTER THESIS

**Study of the temporal properties of the
X-ray emission of the binary system
Her X-1/HZ Her**

Inga SAATHOFF

Hagstrasse 2
72762 Reutlingen
inga.saathoff@student.uni-tuebingen.de

November 2019

Eidesstattliche Erklärung

Hiermit versichere ich, dass ich gemäß des allgemeinen Teils der Studien- und Prüfungsordnung der Universität Tübingen für den Studiengang Physik mit akademischer Abschlussprüfung Master of Science (M.Sc.) vom 30.07.2013 diese Masterarbeit mit dem Titel “Study of the temporal properties of the X-ray emission of the binary system Her X-1/HZ Her” selbstständig verfasst und keine anderen als die angegebenen Hilfsmittel und Quellen benutzt habe. Alle wörtlich oder sinngemäß aus anderen Werken übernommenen Aussagen wurden als solche kenntlich gemacht. Die Arbeit war weder vollständig noch in wesentlichen Teilen Gegenstand eines anderen Prüfungsverfahrens und wurde weder vollständig noch in wesentlichen Teilen bereits veröffentlicht.

Ort, Datum

Unterschrift

Abstract

In this thesis, the X-ray binary system HZ Her/Her X-1 was studied using data from the observatories *NuSTAR* and *HXMT*. Pulse profiles were generated and new features were observed in several cycles: the pulse profiles show a four-peaked structure instead of the two peaked structure that is commonly observed, indicating that the configuration of the X-ray emitting region has changed in these cycles.

In a second part of the work, the so-called pulse profile fitting method was first applied and then analyzed in-depth. The turn-on times were determined, first using a model that the pulse profile shape evolves regularly with a 34.85 d super-orbital cycle and then using a linear regression. In the analysis of the method, several possible issues have been raised, indicating that the method might have shortcomings. This, however, remains an open question. The (O-C) diagrams that were created with the different methods both show a general agreement between the light curve data and the pulse profile fitting method, leading to the conclusion that only one “clock” is present in the system, tentatively confirming the previous results.

Lastly, the pulsed fraction was calculated for the *NuSTAR* data and shows an increase with increasing energy. Also observed were the iron K α line as well as the cyclotron line at about 37 keV.

Contents

List of Figures	ix
List of Tables	xi
1 Introduction	1
1.1 Result Archive	3
1.2 Units	3
1.3 Nomenclature	3
2 Astrophysical Background	5
2.1 X-ray Binaries and Accretion Processes	5
2.1.1 X-ray Binaries	5
2.1.2 Accretion Physics	7
2.1.3 Accretion Columns	9
2.2 The X-ray Binary System Her X-1/HZ Her	12
2.2.1 The System	12
2.2.2 Observational Properties	12
3 The Observatories <i>NuSTAR</i> and <i>HXMT</i>	19
3.1 <i>Nuclear Spectroscopic Telescope Array (NuSTAR)</i>	19
3.1.1 Optics	19
3.1.2 Detectors	20
3.1.3 Mast	20
3.2 <i>Hard X-ray Modulation Telescope (HXMT)</i>	21
3.2.1 High Energy Telescope	22
3.2.2 Medium Energy Telescope	22
3.2.3 Low Energy Telescope	22
4 Data Analysis & Results	23
4.1 Data Reduction	23
4.1.1 <i>NuSTAR</i>	23
4.1.2 <i>HXMT</i>	25
4.2 Data Processing	26
4.2.1 PI to Energy Conversion	26
4.2.2 Spin Period	26
4.2.3 Event folding	29
4.3 Results	31
4.3.1 Energy-Phase Matrices	31
4.3.2 Pulse Profiles	34
4.3.3 Pulse Profile Fitting and (O-C) diagram	40

4.3.4	Analysis of the Pulse Profile Fitting Method	44
4.3.5	Pulsed Fraction	54
5	Discussion & Conclusions	57
35 d	Phases	59
	Bibliography	63

List of Figures

1.1	Illustration of an accreting pulsar.	2
2.1	Schematic view the subclasses of X-ray binaries.	6
2.2	Illustration of accretion geometries.	8
2.3	Schematic illustration of equipotential surfaces in a binary system.	8
2.4	Schematic illustration of an accretion funnel.	10
2.5	Illustration of different geometries of the accretion column.	11
2.6	Illustration of the fan and pencil beam.	11
2.7	Typical X-ray light curve of Her X-1.	13
2.8	Pulse profile nomenclature.	14
2.9	Pulse profile of Her X-1 in different energy ranges.	15
2.10	Pulsed fraction of Her X-1 as function of energy.	15
2.11	(O-C) diagram.	16
2.12	Pulse profile template for the main-on of Her X-1 based on <i>RXTE</i> data.	17
2.13	Pulse profile phase zero determination.	17
3.1	The <i>NuSTAR</i> satellite and its detector.	20
3.2	The <i>HXMT</i> satellite.	21
3.3	Diagrams of the <i>HXMT</i> HE, ME and LE units.	22
4.1	Light curve of a <i>NuSTAR</i> observation including a dip.	24
4.2	Spin period determination.	27
4.3	Definition of the sharp edge.	29
4.4	Example matrix of the <i>NuSTAR</i> observations.	31
4.5	Matrix of the <i>NuSTAR</i> observation 90102002002, cycle 457.	32
4.6	<i>HXMT</i> matrix of observation P0101308001, cycle 477, segment 1.	33
4.7	Pulse profiles of <i>NuSTAR</i> observations from cycle 468 and 478.	35
4.8	Pulse profiles of <i>HXMT</i> observations from cycle 484 and 487.	36
4.9	Comparison of <i>HXMT</i> and <i>NuSTAR</i> pulse profiles of cycles 478 and 484.	37
4.10	Comparison of <i>HXMT</i> and <i>NuSTAR</i> pulse profiles of cycles 494 and 495.	38
4.11	Examples of the template fitting.	40
4.12	Determination of O ^{PP} on the basis of <i>NuSTAR</i> data.	42
4.13	Determination of O ^{PP} on the basis of <i>HXMT</i> data.	43
4.14	Updated (O-C) diagram, assuming a 34.85 d model.	44
4.15	The separate and combined (O ^{LC} -C) and (O ^{PP} -C) diagrams.	45
4.16	Results of cycle 478 from both <i>NuSTAR</i> and <i>HXMT</i> data.	46
4.17	Zero phase determination based on pulse profile fitting data using a fixed slope of 34.85 d as compared to a fit with a free slope parameter.	47
4.18	Determination of O ^{PP} on the basis of <i>NuSTAR</i> data, free fit.	48
4.19	Determination of O ^{PP} on the basis of <i>HXMT</i> data, free fit.	49

4.20 Updated (O-C) diagram, free fit.	51
4.21 ϕ^{PP} vs. ϕ^{LC} plot including uncertainties.	52
4.22 ϕ^{PP} vs. ϕ^{LC} plot including histograms of each.	53
4.23 Pulsed fraction definitions.	55
4.24 Pulsed fraction as a function of energy and 35 day phase.	55
4.25 Pulsed fraction as a function of energy.	56

List of Tables

2.1	Comparison of different typical characteristics of HMXBs and LMXBs.	6
3.1	Key performance parameters of <i>NuSTAR</i>	19
3.2	Key performance parameters of <i>HXMT</i>	21
4.1	Summary of the <i>NuSTAR</i> observations.	24
4.2	Summary of the <i>HXMT</i> observations.	25
4.3	Cycle numbers and relative spin periods of the <i>NuSTAR</i> observations. .	28
4.4	Cycle numbers and relative spin periods of the <i>HXMT</i> observations. .	28
4.5	Energy bins of the pulse profiles.	34
4.6	Spin periods as determined from the <i>NuSTAR</i> and <i>HXMT</i> data for cycles 478, 484, 494 and 495.	39
4.7	Inferred cycle lengths.	48
4.8	Zero phase and (O-C) results of the <i>NuSTAR</i> observations.	50
4.9	Zero phase and (O-C) results of the <i>HXMT</i> observations.	50
1	Results for the 35 d phases of the <i>NuSTAR</i> data.	59
2	Results for the 35 d phases of the <i>HXMT</i> data.	60

Introduction

Stars are not eternal. Main sequence stars are in a state of hydrostatic equilibrium where the inward gravitational force is balanced by an outward thermal pressure, which is caused by nuclear fusion. When the fuel for fusion, mostly hydrogen, runs out, the core of the star collapses. Depending on the initial mass and the metallicity of the previous star, what remains after the collapse is either a white dwarf, a neutron star or a black hole. These states are therefore also called the endpoints of stellar evolution.

In the case of a neutron star, the collapse is stopped by the neutron degeneracy pressure. This pressure can be explained according to quantum mechanics by the Pauli exclusion principle, which states that identical fermions cannot occupy the same quantum state. The degeneracy pressure does not vanish even at absolute zero (Lipunov 1987; Longair 2011).

Most stars have a non-zero rotational velocity and during the core collapse, angular momentum is conserved and the rotation rate therefore increases. Similarly, the magnetic flux is also conserved. Therefore, neutron stars can rotate rapidly and they can have magnetic fields of the order of 10^{12} G (Courvoisier 2013, an references therein).

The first observational confirmation that neutron stars exist came in 1967 from A. Hewish and his graduate student J. Bell, who observed a periodic radio pulse every 1.377 s. This was the first detected radiopulsar: a magnetized neutron star spinning with a period of about 1 second.

When a pulsar is, however, part of a binary system with a normal star, matter can pass from the normal star to the neutron star and eventually be accreted onto its surface. Zel'dovich & Shakura (1969) showed that an accreting neutron star radiates in the X-ray energy range and therefore, so-called X-ray pulsars can be observed in binary systems. A sketch of an accreting pulsar can be seen in Figure 1.1.

A pulse profile shows the detected photons when folding a light curve with the neutron star's pulse period. The shape of a pulse profile depends on many factors, such as the geometry of the emitting region, and it holds information about the distribution of the radiation. The pulse profile can change its shape with energy because, for example, matter is hotter closer to the neutron star surface and this radiation is shielded by the neutron star itself for most of the spin period (Basko & Sunyaev 1976). But it also depends on the density of the accretion column, the pressure at different heights of the accretion column and the accretion geometry itself as well as many other parameters.

Pulse profiles are generally classified as either single- or double-peaked. In some cases, it is interpreted that this depends on if the observer can see either one or both magnetic poles, when assuming a dipole magnetic field. At low energies, the difference is generally not as distinct as at higher energies, above about 10 keV (Lutovinov & Tsygankov 2009).

Some of the most important contributions to understanding the nature of the observational properties listed above are based on the study of X-ray pulsars, in particular

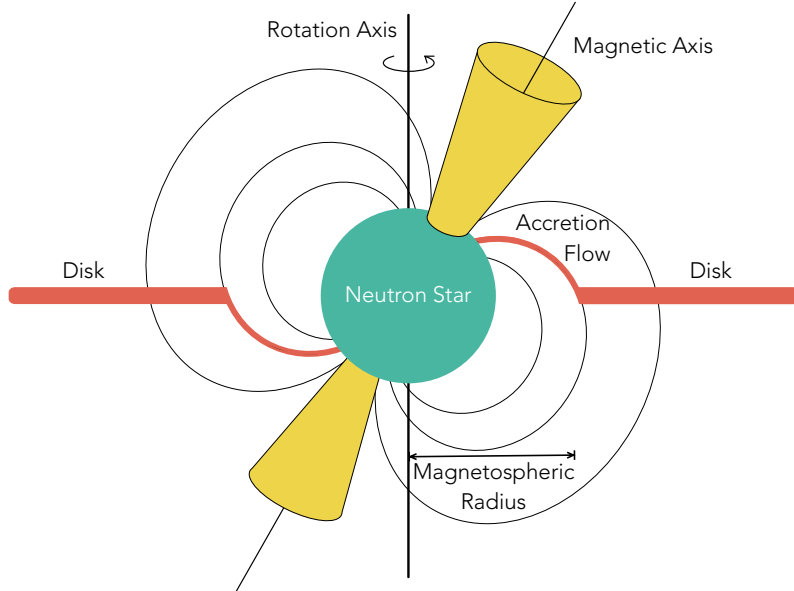


Figure 1.1: Illustration of an accreting pulsar. Matter that is gravitationally captured by a neutron star from a companion can form an accretion disk. As the matter approaches the neutron star, it is then channeled via the magnetic field lines to the magnetic poles of the neutron star. At the poles it can release its gravitational energy and emit thermal radiation in directional beams.

Hercules X-1 (Her X-1). The discovery of periodic X-ray pulsations in the constellation Hercules was first reported by Tananbaum et al. (1972). The 1.24 s pulsations were found to change sinusoidally which was interpreted as due to the Doppler effect and intensity variations were attributed to the occultation by a companion star. The orbital period was found to be about 1.7 d and a super-orbital period was found on a \sim 35 d timescale. Her X-1 was judged to be similar to the occulting binary Cen X-3.

The aim of this thesis is to study the X-ray pulse profiles of Her X-1 based on *NuSTAR* and *HXMT* data and investigate their evolution on the super-orbital timescale. First, in Sections 1.2 and 1.3 the units and common nomenclature in this field of work will be introduced, respectively. In Chapter 2, the astrophysical context will be explored, including an introduction to X-ray binaries and accretion physics in Section 2.1 and the system containing the X-ray pulsar Her X-1 will be described in Section 2.2, including its observational properties.

Chapter 3 portrays the observatories *NuSTAR* and *HXMT* and the most important characteristics for this work of each telescope will be presented. The data analysis and results of the present thesis will be shown in Chapter 4: the data reduction is described in Section 4.1 and a further data processing is shown in Section 4.2. Section 4.3 presents energy-phase matrices which were then further binned in energy to create pulse profiles. These profiles are shown for both *NuSTAR* and *HXMT* data and the further analysis is conducted. Chapter 5 then discusses and summarizes the results.

1.1 Result Archive

Since this thesis contains a “mass production” of energy-phase matrices and pulse profiles, not all results could be printed. In total, more than 300 plots were created. These consist of:

- *NuSTAR*:
 - 42 matrices (in 10 files),
 - 42 pulse profiles and
 - 42 pulse profiles in comparison with the *RXTE* template.
- *HXMT*:
 - 71 matrices,
 - 71 pulse profiles and
 - 71 pulse profiles in comparison with the *RXTE* template.

and they can be retrieved under

https://gitlab.com/isaathoff/master_thesis_results.

1.2 Units

In this thesis, physical quantities are given in the centimeter-gram-second (cgs) system of units, which is common to astrophysics, with a few exceptions. Photon energies are given in keV, where $1 \text{ keV} \approx 1.6 \times 10^{-9} \text{ erg}$. Thus the X-ray waveband refers to an energy range of about 0.1 to 100 keV (Longair 2011). Distances to sources are stated in kpc with $1 \text{ kpc} \approx 3.1 \times 10^{21} \text{ cm}$. Masses and radii are indicated in solar masses (M_{\odot}) and solar radii (R_{\odot}), respectively, where $1 M_{\odot} \approx 1.99 \times 10^{33} \text{ g}$ and $1 R_{\odot} \approx 6.96 \times 10^{10} \text{ cm}$. Notations such as μ_{30} denote the order of magnitude of the corresponding quantity, thus μ_{30} is in units 10^{30} G cm^3 . Dates are given in the Modified Julian date (MJD) system, based on the Julian date (JD), which is an integer counter of the days beginning with 0 at noon, January 1, 4713 B.C. in Greenwich. MJD modifies the JD system by beginning count at midnight instead of noon and removing the first two digits, thus the conversion is $\text{MJD} = \text{JD} - 2400000.5$.

1.3 Nomenclature

X-ray source nomenclature has changed over time and the oldest sources were named according to the nearest constellation, for example Hercules X-1 (Her X-1). Newer sources are designated by their celestial coordinates: Sources in the galactic plane are signified by their galactic longitude and latitude, such as GX 1+4 which lies near $l \approx 1^\circ$ and $b \approx +4^\circ$. More recent and accurate measurements determine the source to be at $l = 1.937^\circ$ and $b = +4.795^\circ$. Other sources are known by a prefix indicating the satellite which discovered the source followed by their right ascension (α) and declination (δ), for example OAO 1657-415, which was discovered by the Copernicus Orbiting Astronomical Observatory 3 (OAO) satellite and lies near $\alpha \approx 16^{\text{h}} 57^{\text{m}}$, $\delta \approx -41^\circ 5'$. The position of this source was later also more accurately determined to be at $\alpha = 16^{\text{h}} 57^{\text{m}} 17.819^{\text{s}}$ and $\delta = -41^\circ 34' 57.99''$.

Astrophysical Background

In a wider astrophysical context, this thesis is concerned with X-ray binaries (XRBs), accretion mechanisms and accretion columns. In particular, the X-ray pulsar Hercules X-1 (Her X-1) will be studied with respect to its observational properties. These topics will be covered in the present chapter as follows.

An introduction to XRBs and the physical mechanisms of accretion will be described in Section 2.1. This includes a brief classification of XRBs, the description of different accretion geometries and an introduction to accretion columns. The contents of this chapter are mainly based on Courvoisier (2013) and Longair (2011). In a second part of the chapter, Section 2.2, the XRB system HZ Her/Her X-1 will be introduced with its observational properties, such as its light curve and characteristic X-ray pulse profile.

2.1 X-ray Binaries and Accretion Processes

The X-ray sky has many different sources that generate X-rays through a variety of physical processes. A population of bright (up to $\sim 10^{38} \text{ erg s}^{-1}$) galactic sources are X-ray binaries (XRBs). XRBs are binary systems consisting of a compact object and a companion star. Different subcategories can be defined depending on the type and mass of these orbiting objects and these will be introduced in Section 2.1.1. The manner, in which matter can transfer from the companion star to the compact object (in this thesis, the compact object is generally assumed to be a neutron star, abbreviated NS) is summarized as accretion physics in Section 2.1.2 and the processes at the NS surface, where matter is falling onto the NS, are covered in Section 2.1.3.

2.1.1 X-ray Binaries

In Figure 2.1, a schematic view of the different types of XRBs is shown. When the compact object is a white dwarf, the binary system is typically a cataclysmic variable. If, however, the compact object is something other than a white dwarf, a further distinction is based on the mass of the companion star (also called the donor or normal star). When the companion star is a massive O or B star, with a mass greater than about $6 M_{\odot}$, the system is called a high mass X-ray binary (HMXB). Systems in which the companion star has a mass smaller than the mass of the sun are dubbed low mass X-ray binaries (LMXBs). HMXBs and LMXBs display several different characteristics, which will be described in the following and are summarized in Table 2.1.

Since high mass stars have shorter lives compared to stars with smaller masses, HMXB are typically associated with young systems and they are found in star forming regions in the disk of our Galaxy. LMXBs, on the other hand, are generally older and can be found not only in the disk but also at other Galactic latitudes, in globular clusters and in the Galactic bulge.

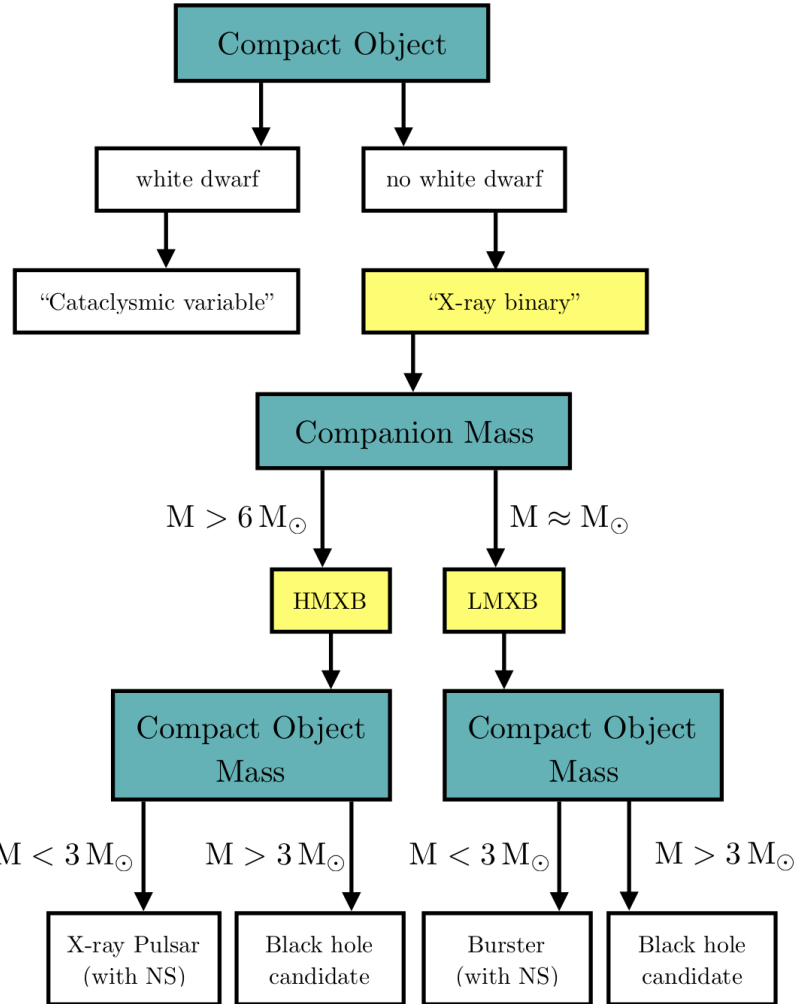


Figure 2.1: Schematic view the subclasses of X-ray binaries. Adapted from Courvoisier (2013).

Table 2.1: Comparison of different typical characteristics of HMXBs and LMXBs.

Parameter	HMXB	LMXB
Companion mass	$M > 6 M_{\odot}$	$M \leq M_{\odot}$
Age of the system	Typically younger	Typically older
Distribution in the Galaxy	Galactic plane	Everywhere
Magnetic fields of compact object	$\sim 10^{12} \text{ G}$	$< 10^{11} \text{ G}$
Accretion mechanism	Stellar wind	Roche lobe overflow
Pulsations	X-ray pulsar	Typically not observed

Another difference between HMXBs and LMXBs is the magnetic field of the compact object, given that the compact object is a NS. In HMXBs, the NS typically has magnetic fields of the order 10^{12} G, whereas in LMXBs, the magnetic fields are typically of the order 10^8 G to 10^{10} G.

The different accretion mechanisms will be described in more detail in Section 2.1.2 but let it be said here that HMXBs typically accrete from a stellar wind and the accreted matter in LMXBs reaches the compact object through Roche lobe overflow.

Lastly, HMXBs and LMXBs present distinct phenomenologies based on the previously discussed differences. Since the NS in HMXBs has a high magnetic field, the accretion of matter is tied to this field even far from the NS. Matter from the companion star will be captured and channeled along the magnetic field lines onto the magnetic poles of the NS. When it reaches the surface of the NS, the gravitational energy is released in the X-ray energy range extending from about 0.1 keV to a few hundred keV. Assuming that the magnetic axis is misaligned with respect to the rotation axis, the observed X-ray flux will change with time as the NS spins. Therefore, the NS in XRBs are often observed as X-ray pulsars.

Because the magnetic fields of NSs in LMXBs are much lower, matter is generally not channeled along the magnetic field lines to the NS surface. Instead, the matter is accreted more uniformly and the observed flux is not modulated with the NS spin (Courvoisier 2013).

2.1.2 Accretion Physics

As previously mentioned, matter can be accreted in an XRB through two main mechanisms. HMXBs mainly accrete matter from a stellar wind and LMXBs typically through Roche lobe overflow. In the following, these processes, also illustrated in Figure 2.2, will be described. The contents of this section is mainly based on Longair (2011) and Shapiro & Teukolsky (1983).

Roche Lobe Overflow

The equipotential surfaces of a binary system are schematically illustrated in Figure 2.3. In the rotating frame of reference of a binary system, these surfaces are defined where the potential

$$\phi = \frac{GM_1}{r_1} + \frac{GM_2}{r_2} - \Omega^2 r^2$$

is constant. Here r_1, r_2 are the distances of the stars with mass M_1, M_2 and Ω is the angular velocity of the system. As seen in the figure, the equipotential surfaces are spherical around the center of mass far from the stars and also close to each of the stars. In-between these two limits, the surfaces get deformed and the smallest common envelope is called the Roche lobe. In the system, there are five points of equilibrium, dubbed Lagrangian points L_1 to L_5 . The Lagrangian point L_1 is located between the two stars.

During the course of its evolution, the companion star might expand and get deformed to fill its Roche lobe. When this happens, matter can pass through the inner Lagrangian point L_1 and is gravitationally captured by the compact object. If the matter has sufficient angular momentum, an accretion disk can form from which it is then accreted onto the compact object.

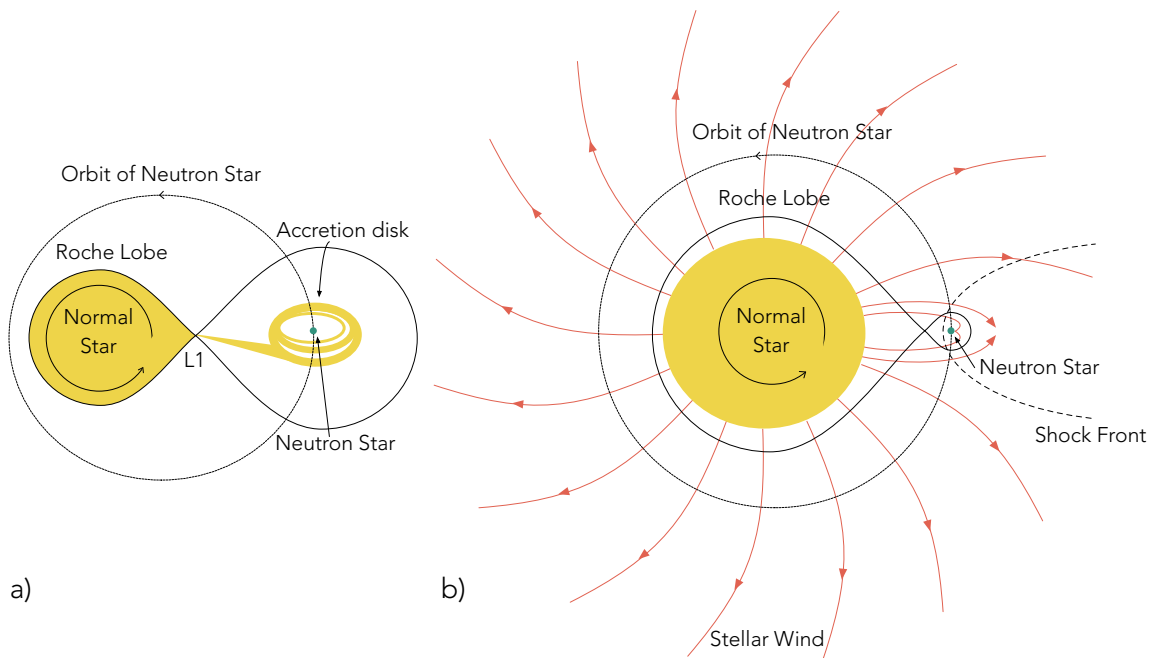


Figure 2.2: Illustration of accretion geometries. In scenario a) the normal (donor) star expands and fills its Roche lobe. Matter then passes through the Lagrangian point L1 to the NS. In scenario b) the NS is embedded in the strong stellar wind of the normal star from which it is accreting. Adapted from Shapiro & Teukolsky (1983).

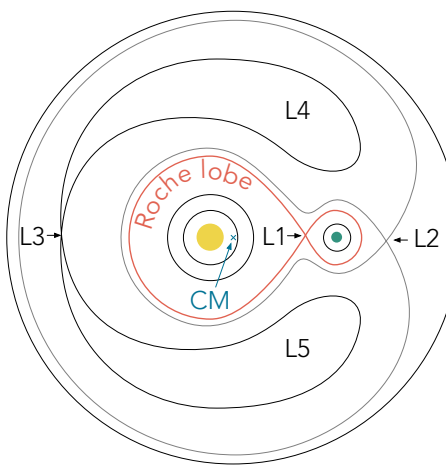


Figure 2.3: Schematic illustration of equipotential surfaces in a binary system with different masses. The surfaces are spherically symmetric in close proximity to each star as well as at a large distance around the center of mass (CM). Between these limits, they are deformed. The smallest common envelope is called the Roche lobe and the five equilibrium points, labeled L1 to L5, are dubbed Lagrangian points.

Wind Accretion

In the wind accretion case, the Roche lobe is not filled by the companion star. Luminous O and B class stars, which are typical in these systems, are known to have strong stellar winds. When the compact object is embedded in this wind, see Figure 2.2, it can capture matter directly. Only about 0.1% of the ejected matter can be accreted in this case. When matter is accreted from a stellar wind, accretion is assumed to be mostly spherical, but an accretion disk may also form if the angular momentum of the matter is sufficient.

2.1.3 Accretion Columns

So far, the different types of XRBs have been introduced and scenarios of how matter is transferred from the companion toward the compact object have been explained. In the following, the way in which the matter can then reach the surface of the NS and be accreted will be described in more detail. The content of this section is based on Shapiro & Teukolsky (1983).

The magnetic fields in accreting NSs can control the way in which matter flows to the NS's surface. The magnetic field does not influence the matter at a great distance from the NS. Close to it, however, the magnetic field dominates the plasma flow. The Alfvén radius, r_A , is defined where the magnetic energy density is equal to the kinetic energy density of the accreted matter. In terms of the accretion luminosity L , r_A is

$$r_A = 3.5 \times 10^8 L_{37}^{-2/7} \mu_{30}^{4/7} (M/M_\odot)^{1/7} R_6^{-2/7} \text{ cm}, \quad (2.1)$$

where μ_{30} is the magnetic moment in units of 10^{30} G cm^3 , R_6 is the NS radius in units of 10^6 cm and L_{37} is in units of $10^{37} \text{ erg s}^{-1}$.

The exact process how the accreted matter penetrates the magnetosphere or is channeled by the magnetic field onto the NS surface is a very complex problem. Qualitatively speaking, a standing shock develops close to the Alfvén surface, which inhibits the accretion flow. Inside r_A , the matter is believed to be tunneled in a narrow accretion column onto the surface. The magnetic field lines of a dipole field are defined by

$$\frac{\sin^2 \theta}{r} = \text{const.}, \quad (2.2)$$

where r is the distance from the NS and θ is the angle between r and the dipole field. The magnetic pole region is bounded by the last magnetic field lines that are closed in radii smaller than r_A , see Figure 2.4, and defined by the critical angle θ_c given by

$$\sin^2 \theta_c = \frac{R}{r_A} \approx 3 \times 10^{-3} [R_6^{9/7} L_{37}^{2/7} \mu_{30}^{-4/7} (M/M_\odot)^{1/7}] \quad (2.3)$$

when using Equation 2.1 for r_A . Therefore, the polar region at the base of the accretion column will be

$$A \approx \pi R^2 \sin^2 \theta_c \approx 10^{10} \text{ cm}^2, \quad (2.4)$$

which is only a fraction of the total surface of the NS (assuming a NS radius of 10 km the surface is about 10^{13} cm^2).

Later works proposed that a Rayleigh-Taylor instability might cause blobs of plasma to enter the magnetosphere and be accreted, as opposed to a threaded matter flow

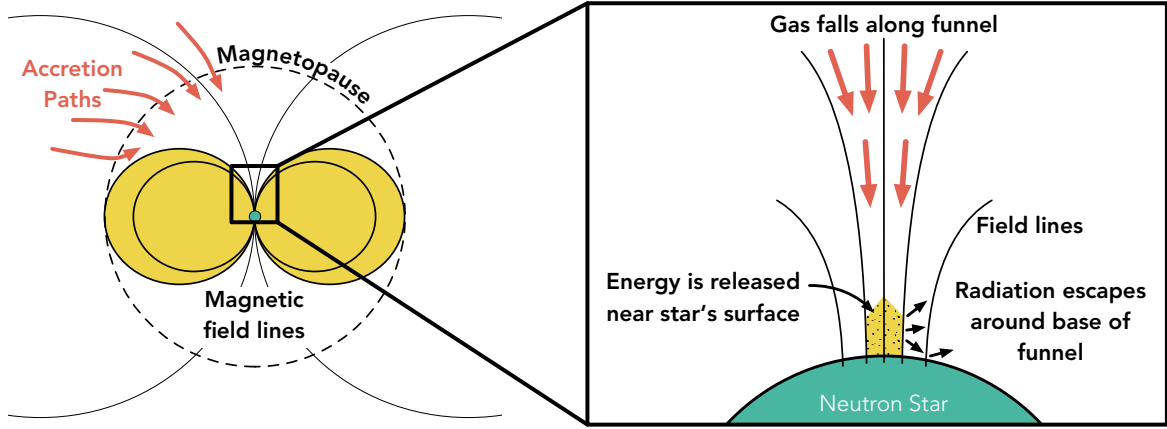


Figure 2.4: Schematic illustration of an accretion funnel. The magnetopause is the boundary between the magnetosphere and the surrounding matter. Adapted from Shapiro & Teukolsky (1983).

onto the poles of the NS. This would lead to a much larger polar region, but the exact processes are not fully understood.

How exactly matter is latched to the field lines is also not clear, and the extent of the “threading” region would determine if the accretion column is a filled cylinder or a hollow funnel. Instabilities could also cause the matter to break up into blobs or closer to the polar cap into pancake or spaghetti shapes, see also Figure 2.5 (Basko & Sunyaev 1976; Meszaros 1984).

When the matter finally reaches the pole of the NS, there are two possible structures of the emitting region. For low accretion rates and low X-ray luminosities, $L_x \leq 10^{37} \text{ erg s}^{-1}$, matter is decelerated through Coulomb scattering with electrons in the NS atmosphere. The X-rays can then escape radially, leading to the formation of a so-called pencil beam. At high accretion rates, however, the radiation pressure dominates the gas pressure and the accreted matter loses its energy in a radiation dominated shock. In this scenario, the X-rays are emitted toward the sides of the accretion column and the beam geometry is dubbed a fan beam, see also Figure 2.6.

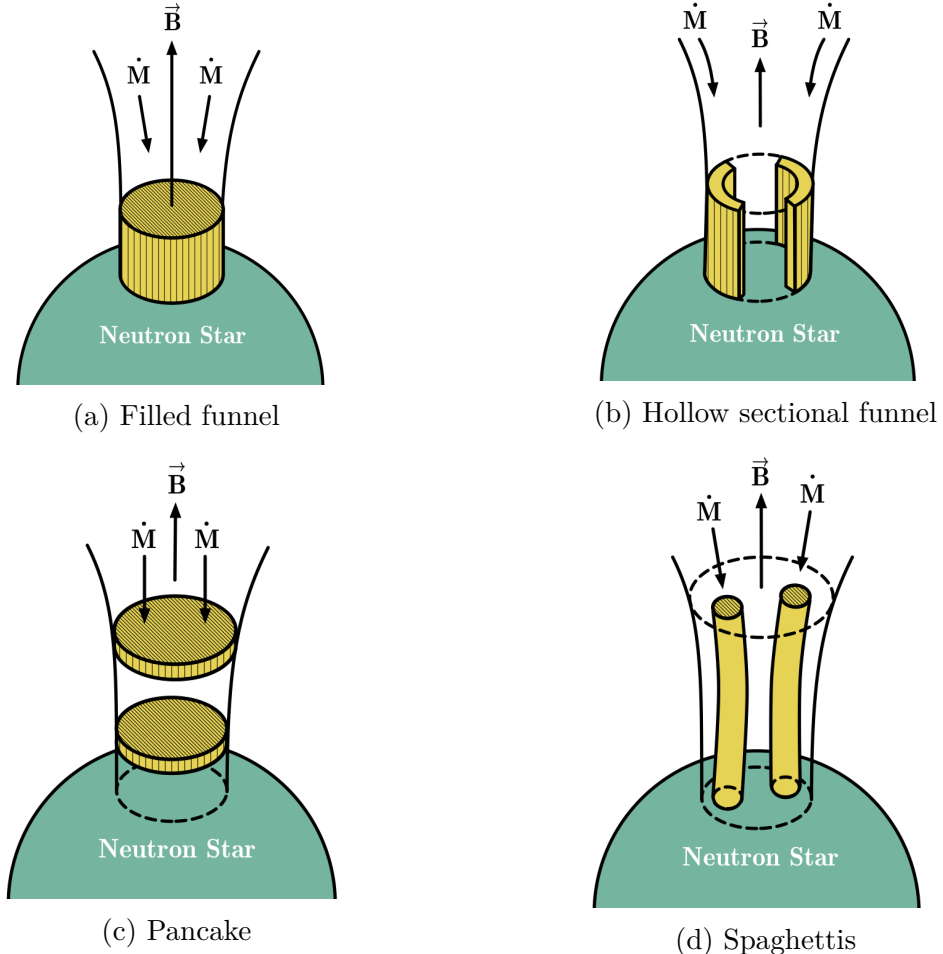


Figure 2.5: Illustration of different geometries of the accretion funnel or column.
Adapted from Basko & Sunyaev (1976); Meszaros (1984).

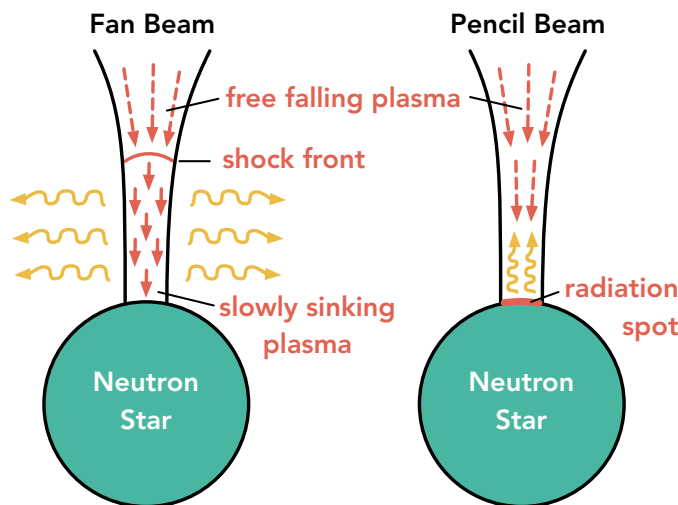


Figure 2.6: Illustration of the fan and pencil beam. In the fan beam, as seen on the left hand-side, a shock is generated and radiation is emitted sideways. When no shock is present, radiation can escape upwards, giving rise to the so called pencil beam, shown on the right side. Adapted from Basko & Sunyaev (1976); Meszaros (1984).

2.2 The X-ray Binary System Her X-1/HZ Her

The present thesis will analyze Hercules X-1, which is an XRB system consisting of a pulsar (Her X-1) and a companion star (HZ Her). In this section, the XRB system HerX-1/HZ Her will be introduced and its main observational properties, such as its light curve, pulse profile and spectrum, are described. The introductory information is mainly based on Shapiro & Teukolsky (1983).

2.2.1 The System

Her X-1 was first classified as an X-ray source by Tananbaum et al. (1972) and since then the Her X-1/HZ Her system is one of the brightest and best studied X-ray binary systems. It is variable on three different timescales: the NS is spinning with a period of about 1.24 s, the binary period is 1.7 d and a super-orbital “on-off” cycle is observed on a timescale of about 35 d.

The binary system is located in the constellation Hercules at a right ascension of $6^h 57' 50''$ and a declination of $+35^\circ 20' 33''$ ¹ at a distance of (6.6 ± 0.4) kpc (Reynolds et al. 1997). Leahy & Abdallah (2014) place the system at $6.1^{+0.9}_{-0.4}$ kpc. A more precise value for the binary orbit is $1.700\,167\,590(2)$ d. This and further orbital parameters can be found in Staubert et al. (2009b).

The companion star HZ Herculis shows optical pulsations with the same 1.24 s period as the NS spin. These pulsations are explained by the absorption and heating of the pulsed X-ray emission from Her X-1 by HZ Her. The mass of the NS is (1.5 ± 0.3) M_\odot and the mass of the companion is (2.3 ± 0.3) M_\odot with a radius of (4.2 ± 0.2) R_\odot and spectral type B3-B4F (Reynolds et al. 1997). A more recent study by Leahy & Abdallah (2014) derived a mass of HZ Her between either $(2.15 - 2.20)$ M_\odot or $(2.35 - 2.45)$ M_\odot , implying a NS mass of $1.3 M_\odot$ or $(1.5 - 1.7)$ M_\odot , respectively. Due to the mass of the companion star, the system lies between the definitions of LMXBs and HMXBs (see also Section 2.1) and is therefore sometimes called an intermediate X-ray binary (IXRB). The accretion mechanism in this system is, however, most likely through Roche lobe overflow, which is typical for LMXBs.

2.2.2 Observational Properties

Some of the observational properties of the Her X-1/HZ Her system will be introduced in the following, including descriptions of the light curve and pulse profile.

Light Curve

A typical 35 d cycle of Her X-1/HZ Her, also known as the “35 day on-off cycle”, can be seen in Figure 2.7. This super-orbital period is associated with a precessing warped accretion disk (Staubert et al. 2017, and references therein). The modulation in flux is classified into the so-called on-state and off-state, where a high or low flux is detected, respectively. The on-states can further be divided into a main-on and a short-on state. During the main-on, the detected X-ray flux is about four to five times higher than during short-on. The main-on lasts about 7 orbital cycles, while the short-on lasts 5

¹<https://heasarc.nasa.gov/cgi-bin/Tools/convcoord/convcoord.pl>

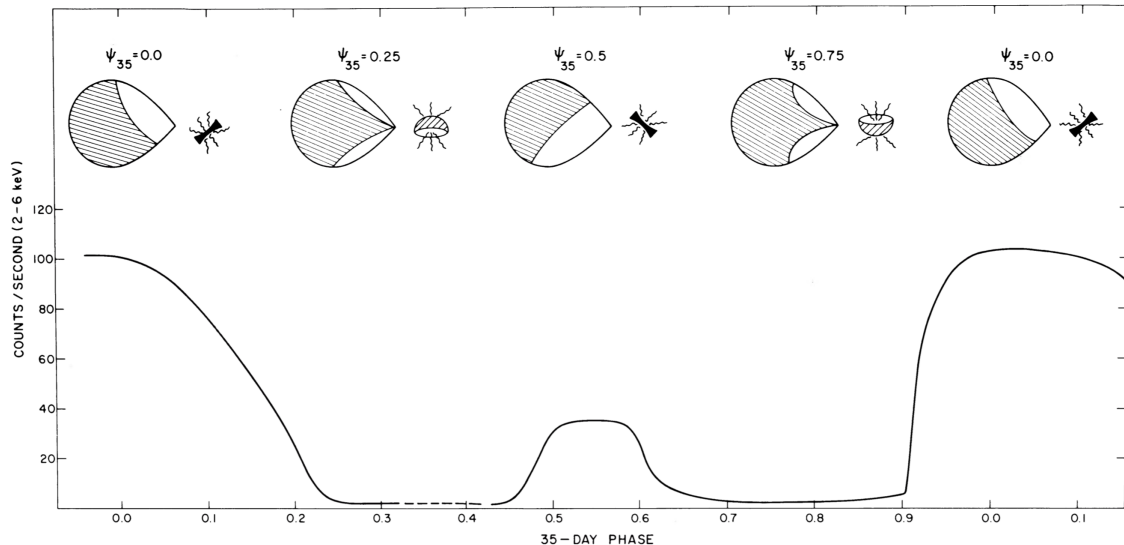


Figure 2.7: Typical X-ray light curve of Her X-1. The on-states are divided into the short-on and the main-on, separated by off-states (Jones & Forman 1976).

orbital cycles, corresponding to about 11 and 8 days, respectively. The off states last 4–5 orbital cycles.

The sharp transition from the off-state to the main-on is the so-called turn-on and it is used to count the 35 d cycles. It is defined at the point when the X-ray flux reaches 10% of the maximum flux of the corresponding main-on. The duration of the 35 d cycle is not always the same and is usually either 20, 20.5 or 21 times the orbital period of 1.7 d.

Pulse Profile

The pulse shape and pulse profiles contain encoded details about the geometric configuration of the emitting region of the pulses. It holds information about the directionality distribution of the radiation. Typically, pulses are single peaked at higher energies and multiple peaked at lower energies. An asymmetric pulse implies an asymmetric emission region or a non-dipolar magnetic field. The pulse profile might also be changed by absorption close to the magnetospheric boundary (Meszaros 1984).

The pulse profile of Her X-1 is known to show a systematic variation with 35 d phase. Observations with *Ginga* and the *Rossi X-ray Timing Explorer (RXTE)* by Scott et al. (2000) show the variation of the features depending on phase and energy. A typical X-ray pulse profile of Her X-1 during a main-on is shown in Figure 2.8 with the nomenclature based on Deeter et al. (1998).

The profile is double-peaked. The larger pulse is called the main pulse and the smaller one is dubbed the interpulse. Before the interpulse, a pre-interpulse minimum is typically observed and the main pulse shows features to the left and right, the leading and trailing shoulders, respectively. For a more comprehensive description of the pulse profiles, see e.g. Deeter et al. (1998) and Scott et al. (2000).

The pulse profile of Her X-1 during main-on changes with time and energy. The main peak becomes narrower as seen in Figure 2.9 (Klochkov et al. 2008). At lower energies, the trailing shoulder is more dominant and the leading shoulder overtakes the main peak in intensity. At higher energies, the sharp edge becomes less steep.

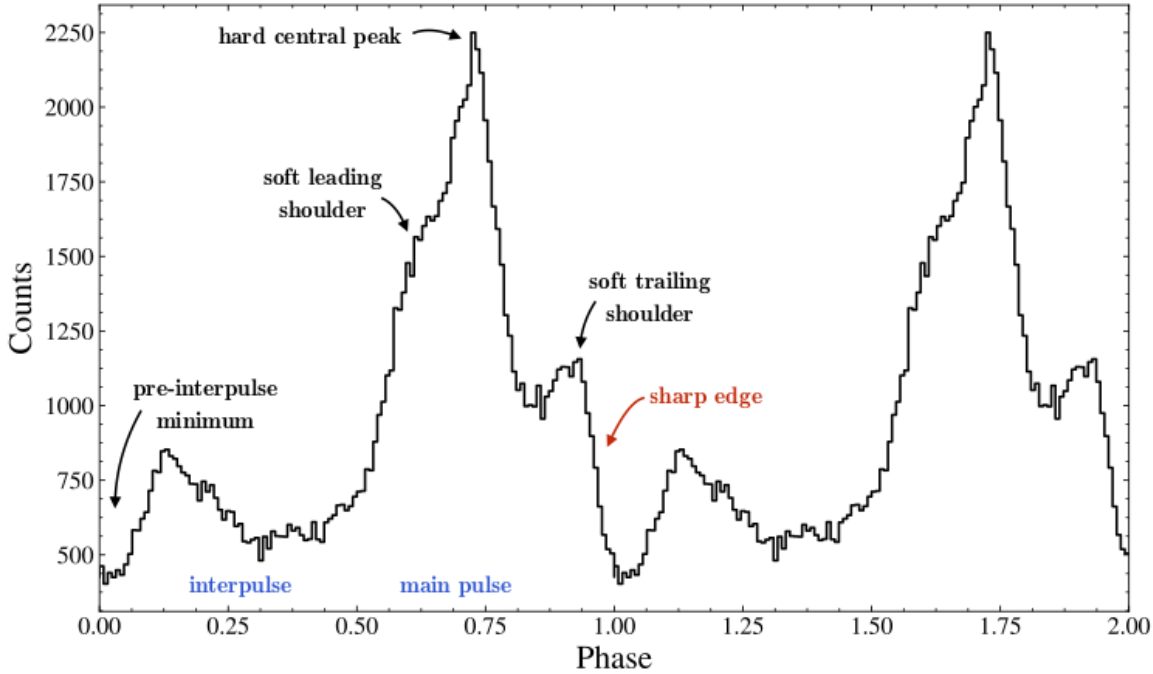


Figure 2.8: Typical X-ray pulse profile of Her X-1 during a main-on state with annotated nomenclature of its main features. The sample shows *NuSTAR* observation 10202002002 at an energy range of 9 to 13 keV. The nomenclature is based on Deeter et al. (1998).

The observed pulse profile shape can be explained by the superposition of the two different beam types, the pencil beam and the fan beam that were introduced in Section 2.1.3 and illustrated in Figure 2.6 (Deeter et al. 1998).

Klochkov et al. (2008) also studied the pulsed fraction as a function of energy and, as seen in Figure 2.10, it increases with energy. This is explained by geometric effects. The soft photons are emitted at the upper part of the accretion column and they are therefore seen during a larger part of the spin period. Harder photons, however, are emitted at the base and screened for most of the spin period (Klochkov et al. 2008).

Turn-on and (O-C) Diagram

As previously mentioned, the turn-on describes the transition between the off-state and the main-on. The 35 d cycles can then be counted. It is convention to count the cycles based on Staubert et al. (1983), where cycle number zero has its turn-on at JD 2 441 325.680. The 35 d super orbital period itself is not constant and the changes over time are shown in the (O-C) diagram, which describes the difference between the observed (O) and the calculated (C) turn-ons, assuming a constant period. The (O-C) diagram has been reported for example in Staubert et al. (2013). An updated diagram with the most recent observed turn-ons can be seen in Figure 2.11.

The time between turn-ons is usually 20, 20.5 or 21 times the orbital period. In Figure 2.11, a period of 34.85 d was assumed to calculate the turn-ons.

In the past, several so-called anomalous lows were observed, where the X-ray flux of Her X-1 was unusually low or not observed at all. During these anomalous lows, turn-ons could not be detected. Staubert et al. (2009a) discuss the third anomalous

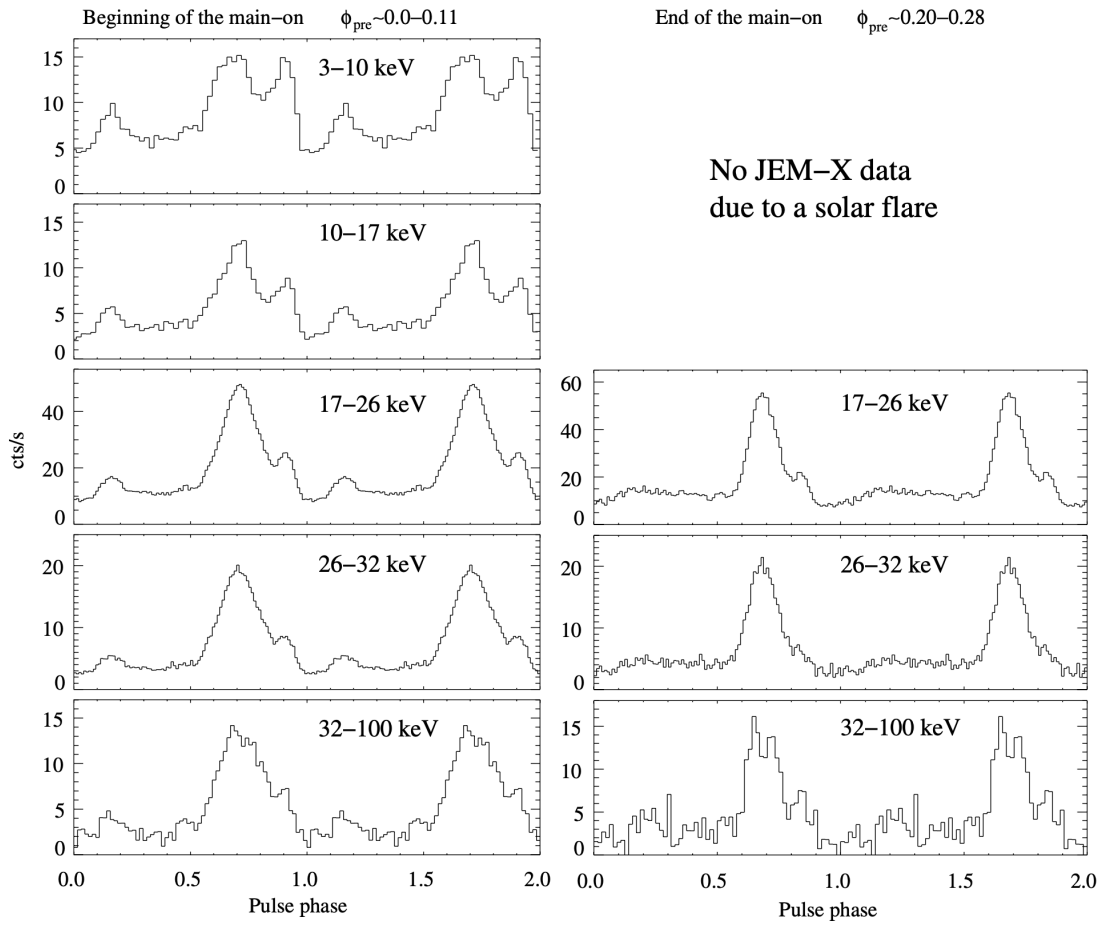


Figure 2.9: Pulse profile of Her X-1 in different energy ranges as observed by *INTEGRAL* (Klochkov et al. 2008).

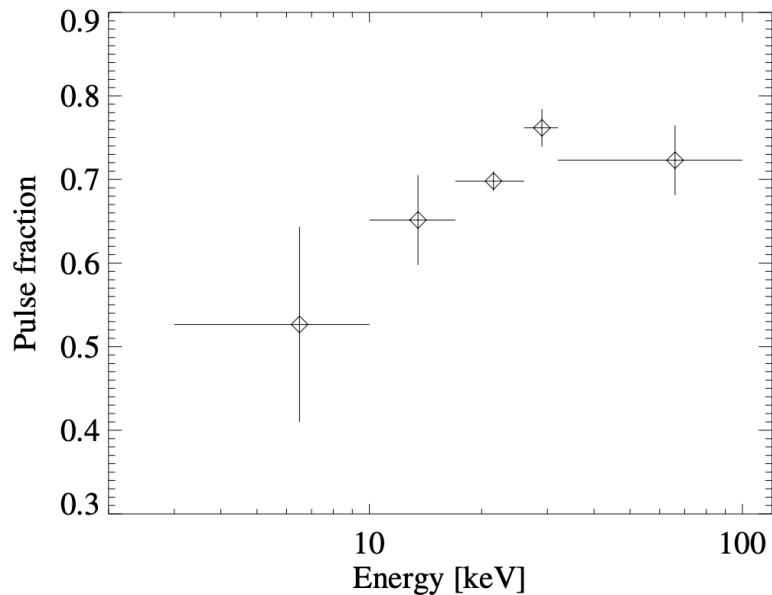


Figure 2.10: Pulsed fraction of Her X-1 as function of energy (Klochkov et al. 2008).

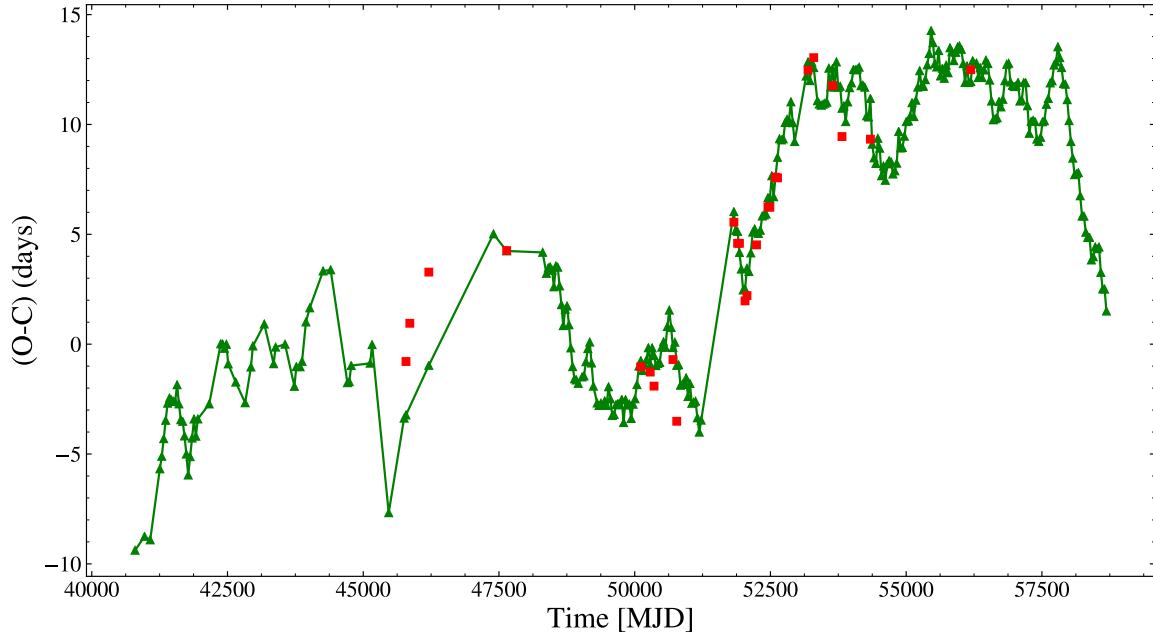


Figure 2.11: The (O-C) diagram for the observed turn-ons (green triangles) and the turn-ons determined from pulse profile fitting (red squares). R. Staubert, private communication 2019.

low, which occurred around MJD 51500. During this time, the number of 35 d cycles that passed could either be 17 or 18, corresponding to 20.8 or 19.7 orbital periods, respectively. In this paper, the solution of 18 cycles is favored and explained by two different “clocks” that act in the system: the “turn-on clock” and the “pulse profile clock”. The turn-on clock is determined by the precession of the accretion disk and the pulse profile clock possibly by a free precession of the NS. Later papers, such as Staubert et al. (2010a,b, 2013), discuss the possibility that there is in fact only one clock present in the system and the solution with 18 cycles is ostensibly the correct one. The pulse profile shows, as previously mentioned, a systematic variation with 35 d phase and was therefore used to create a so-called pulse profile template (Staubert et al. 2010c). A template based on *RXTE* data from 1996 to 2005 can be seen in Figure 2.12. Shown are pulse profiles between 35 d phase 0 and 0.264 with a resolution of 0.002.

Using a template such as this, the turn-on time was derived as follows. The observed pulse profiles were smoothed and normalized to match the template profiles and a χ^2 test determined the best fitting template corresponding to a 35 d phase. With multiple observations in one cycle, as shown in Figure 2.13, the zero phase, corresponding to the turn-on time, was determined by extrapolation and a fixed cycle length of 34.85 d.

The (O-C) diagram was thus complemented with the turn-on times as determined by pulse profile fitting. It was found, as can also be seen in Figure 2.11, that the turn-ons based on pulse profile fitting yield the same results as the observed turn-ons from the light curve and in the (O-C) diagram. The erratic behavior of (O-C) is tracked even on short time scales of a few 35 d cycles. Staubert et al. (2013) then propose a strong feedback interaction model, explaining how a change in the precessional period of the NS can be transmitted to the accretion disk on such small timescales.

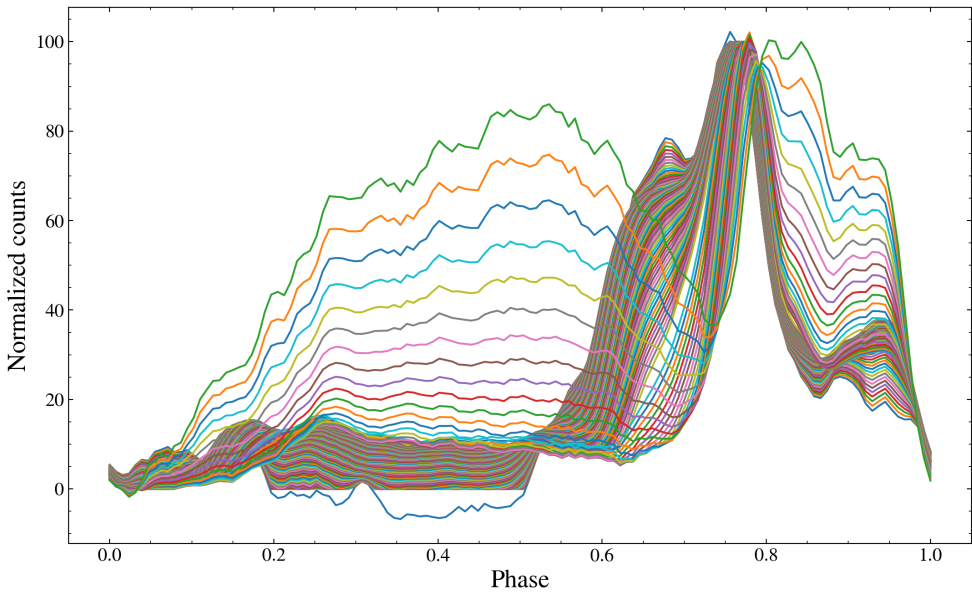


Figure 2.12: Pulse profile template for the main-on of Her X-1 based on *RXTE* data in the 9 to 13 keV energy range (Staubert et al. 2013). Shown are profiles between 35 d phase 0 and 0.264 with a resolution of 0.002. R. Staubert, private communication 2019.

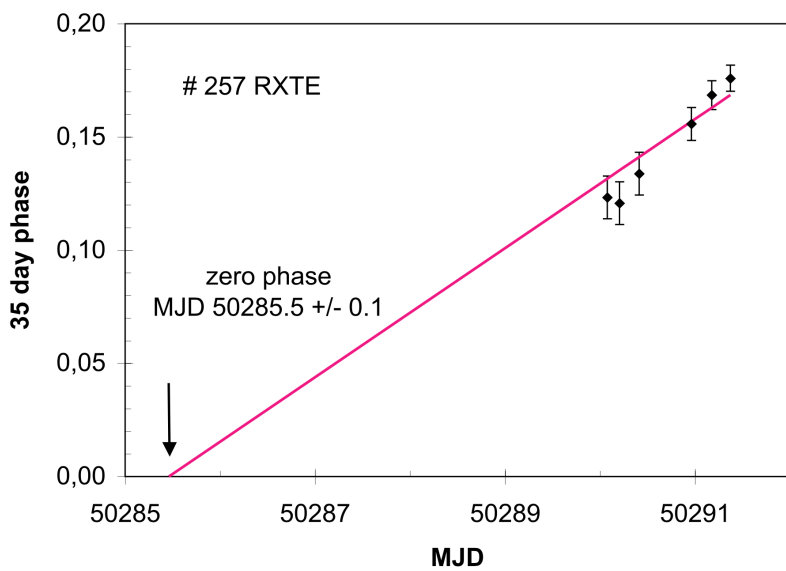


Figure 2.13: Pulse profile phase zero (turn-on time) determination using a fixed cycle length of 34.85 d at the example of cycle 257 with *RXTE* data (Staubert et al. 2013).

The Observatories *NuSTAR* and *HXMT*

3.1 Nuclear Spectroscopic Telescope Array (*NuSTAR*)

The *Nuclear Spectroscopic Telescope Array (NuSTAR)* mission was launched in a near-equatorial, low-Earth orbit on June 13, 2012. It is a Small Explorer (SME) mission of NASA and the first focusing high-energy X-ray telescope, operating in an energy range of 3 to 79 keV. Its main science goals include taking a census of collapsed stars and black holes, mapping recently synthesized material in supernova remnants and investigating relativistic jets of particles in active galactic nuclei.

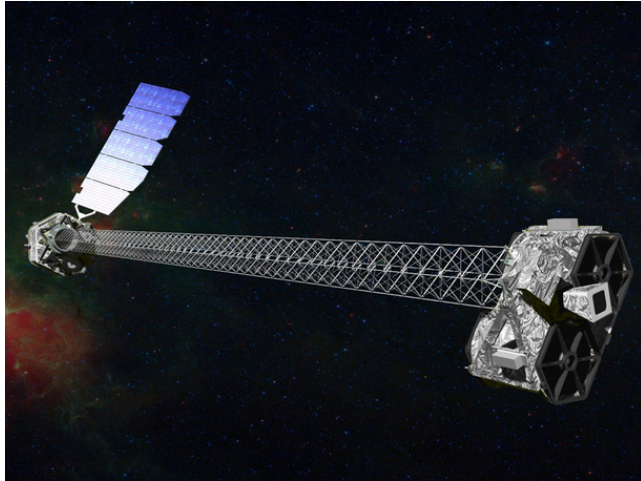
NuSTAR, shown in Figure 3.1a, consists of two co-aligned X-ray telescopes that are positioned on an extendible mast to achieve a focal length of 10.14 m. Each of the two telescopes has its own focal plane module (FPMA and FPMB). Some of the key parameters and characteristics of the instrument are shown in Table 3.1 and the optics, detectors and the mast will be introduced in Sections 3.1.1, 3.1.2 and 3.1.3, respectively. The technical information presented here can be found in Harrison et al. (2013).

Table 3.1: Key performance parameters of *NuSTAR* (Harrison et al. 2013).

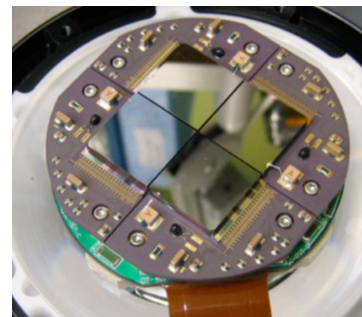
Parameter	Value
Energy range	3 to 79 keV
Energy resolution (FWHM) at 10 keV	400 eV
Energy resolution (FWHM) at 68 keV	900 eV
Angular resolution (FWHM)	18"
FoV (50% resp.) at 10 keV	10'
FoV (50% resp.) at 68 keV	6'
Relative time resolution	2 μ s

3.1.1 Optics

The *NuSTAR* optics consist of two modules with each 133 nested multilayer-coated grazing incidence shells, which are arranged in conical approximation to a Wolter-I telescope geometry. The focal length is 10.14 m and each shell consists of 0.2 mm thin formed glass segments. The inner 89 shells are coated with Pt/C multilayers that reflect efficiently below the Pt K-absorption edge (78.4 keV). The outer 44 shells are



(a) Artist's concept of *NuSTAR* in orbit. The optics are located on a deployable mast, providing a focal length of about 10 m. Courtesy NASA/JPL-Caltech



(b) Photograph of a *NuSTAR* focal plane, consisting of a two-by-two array of CdZnTe pixel detectors (Harrison et al. 2013).

Figure 3.1: (a) The *NuSTAR* satellite and (b) its detector.

coated with W/Si multilayers that efficiently reflect below the W K-absorption edge (69.5 keV).

The effective field of view (FoV) is defined as the furthest off-axis position that has 50% of the on-axis effective area. The FoV decreases with energy and is for *NuSTAR* 10' at 10 keV and 6' at 68 keV. The point-spread function (PSF) is in first order approximation constant with off-axis angle.

3.1.2 Detectors

In the focal plane of the detector are two focal plane modules (FPMA and FPMB), consisting of a solid state CdZnTe pixel detector. There are four detectors that are arranged in a two-by-two array. Each detector has an array of 32×32 pixels and each pixel is 0.6 mm in size, providing a 12' FoV. The detectors measure the arrival time of an X-ray photon with 2 μ s relative time resolution. Also measured is the location, energy, and depth-of-interaction in the detector. The latter measurement can be used to reduce the internal detector background by setting an energy-dependent threshold.

The detectors are surrounded by a CsI anti-coincidence shield. When an event is measured simultaneously in the detector and the shield, the event is rejected as background. Since the opening angle of the shield is large with 15° full width at zero intensity (FWZI), aperture stops were deployed with the mast, collimating the detector to a 4° FWZI field. This field is, however, not completely blocked by the optics bench, which results in stray light, which dominates the background below 10 keV.

3.1.3 Mast

NuSTAR was launched with a stowed mast providing the 10.14 m focal length required. The mast is made of carbon fiber, aluminum and steel and it was deployed in orbit and locked in place with steel cables.

3.2 Hard X-ray Modulation Telescope (HXMT)

The *Hard X-ray Modulation Telescope (HXMT)*, also known as *Insight-HXMT*, is the first X-ray satellite of China and was launched on June 15, 2017 (Zhang et al. 2019). There are three main scientific goals of the *HXMT* mission. First, *HXMT* searches for new transient sources and monitors known variable sources. Second, X-ray binaries are observed to gain a deeper understanding of the physics in strong gravitational and magnetic fields. And lastly, gamma-ray bursts (GRBs) are detected and studied with the satellite.

To achieve these scientific goals, *Insight-HXMT* has three telescopes onboard. The High Energy X-ray telescope (HE), the Medium Energy X-ray telescope (ME) and the Low Energy X-ray telescope (LE). The key characteristics of the telescopes are listed in Table 3.2 and will be discussed in more detail in the following Sections 3.2.1, 3.2.2 and 3.2.3, respectively.¹

Table 3.2: Key performance parameters of *HXMT* (Zhang et al. 2019).

Parameter	Value
HE energy range	20 to 250 keV
HE detection area	5100 cm ²
HE energy resolution	about 14% to 16% at 60 keV
ME energy range	5 to 30 keV
ME detection area	952 cm ²
ME energy resolution (FWHM)	about 3 keV at 20 keV
ME time resolution	244 µs
LE energy range	1 to 15 keV
LE detection area	384 cm ²
LE energy resolution	140 eV at 5.9 keV
LE time resolution	about 1 ms



Figure 3.2: Artist's rendition of *HXMT* in space. Image Credit: Xinhua / SASTIND.

¹The information is based on <http://www.hxmt.org/index.php/enhome/enabouthxmt/160-hard-x-ray-modulation-telescope> (Accessed September 26, 2019)

3.2.1 High Energy Telescope

The high energy (HE) telescope onboard the *HXMT* satellite consists of an array of NaI(Tl)/CsI(Na) phoswich detectors. The field of view (FoV) is $5.2^\circ \times 5.2^\circ$ full width at half maximum (FWHM) and the energy range is 20 to 250 keV. The CsI(Na) part of the detector can also be used as a gamma-ray burst (GRB) monitor. In GRB mode, the energy range is changed to 200 keV to 3 MeV. The HE detector has 18 collimators, arranged in an orientation to confine the FOV and reduce the background. A diagram of a HE detector unit can be seen in Figure 3.3a.

3.2.2 Medium Energy Telescope

The medium energy (ME) telescope observes the energy range of 5 to 30 keV using a Si-PIN detector array with 1728 pixels. A pixel covers an area of 56.25 mm^2 and four pixels together are located in one ceramic package. The ME telescope can be divided into three main parts: the detector, collimator and electronics. A schematic view of the ME detector unit can be seen in Figure 3.3b.

3.2.3 Low Energy Telescope

The low energy (LE) telescope onboard *HXMT* supplements the HE and ME telescopes and covers an energy range of about 1 to 15 keV. The LE telescope uses collimators to reduce background and shield photons outside the FOV and it uses swept charge devices (SCDs) as opposed to charged coupled devices (CCDs), which can work in a continuous readout mode, thus achieving a higher time resolution. The LE contains three identical detector boxes, see Figure 3.3c, and one electric control box. The detector boxes are located at an angle of 120° to each other to enable the modulation of the signals and thus to extract the image information.

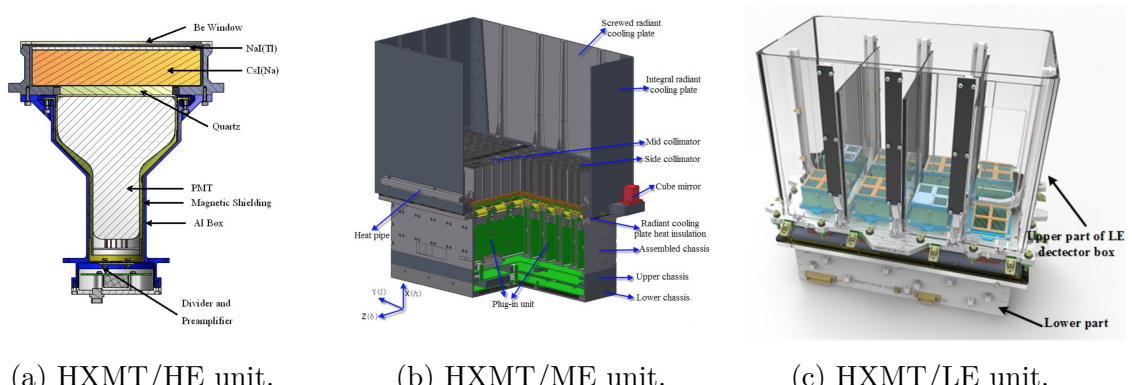


Figure 3.3: Diagram of the HXMT/HE unit and structural designs of the HXMT ME and LE units. Image Credits: hxmt.org

Data Analysis & Results

Her X-1 was observed by the X-ray observatories *NuSTAR* and *HXMT* that were described in Chapter 3. This chapter is dedicated to the description of the data analysis process and the presentation of the results. In the following Section 4.1, the data reduction for both instruments is described, followed by a further data processing in Section 4.2. Finally, the results are presented and discussed in Section 4.3.

4.1 Data Reduction

4.1.1 *NuSTAR*

Her X-1 was observed on numerous occasions between September 2012 and March 2019 by the *NuSTAR* satellite. The individual observation identification numbers (ObsID) and their corresponding start and exposure times are listed in Table 4.1. *NuSTAR* data is made available by the NASA High Energy Astrophysics Science Archive Research Center (HEASARC)¹ and the data of the observations of Her X-1, that are listed in Table 4.1, were retrieved from this archive. The data processing was then conducted in three stages using the *NuSTAR* Data Analysis Software (*NuSTARDAS*)². This package also makes use of HEASARC’s calibration database (*CALDB*), which includes data that is used for the calibration of high energy astronomical instrumentation.

In the first stage of *NuSTARDAS*, the data is calibrated. The calibrated event files are then screened in a second stage. The third stage returns the scientific data products. Each processing stage is made of multiple software modules, including **FTOOLS** (220ct2018_V6.25), which is a part of the **HEASoft** package. The stages were carried out using the *NuSTAR* pipeline (*nupipeline*, 06Oct2016_V0.4.6) script. The solar system barycenter correction was then calculated with the multi-mission **FTOOL** **barycorr**. To retrieve only the events from the source, a circular region file with a 120” radius, centered around the source (RA 16 57 49.81, Dec 35 20 32.5), was created using **SAOimage ds9** (version 8.0.1). Also, a background region was selected at the opposite corner of each image with a radius of 80”. The events were selected using **XSELECT** V2.4f. Since some of the light curves showed dips, good time intervals (GTI’s) were selected manually (see Figure 4.1 as an example) and applied to the event files, also using **XSELECT** V2.4f. Finally, the correction for binary motion was calculated using the orbital data as reported in (Staubert et al. 2009b).

¹The data can be accessed at <https://heasarc.gsfc.nasa.gov/cgi-bin/W3Browse/w3browse.pl>.

²This research has made use of the *NuSTAR* Data Analysis Software (*NuSTARDAS*) jointly developed by the ASI Science Data Center (ASDC, Italy) and the California Institute of Technology (Caltech, USA). For more information about the *NuSTAR* data analysis process, see Perri et al. (2017) at https://heasarc.gsfc.nasa.gov/docs/nustar/analysis/nustar_swguide.pdf and Forster et al. (2014) at https://heasarc.gsfc.nasa.gov/docs/nustar/analysis/nustar_quickstart_guide.pdf.

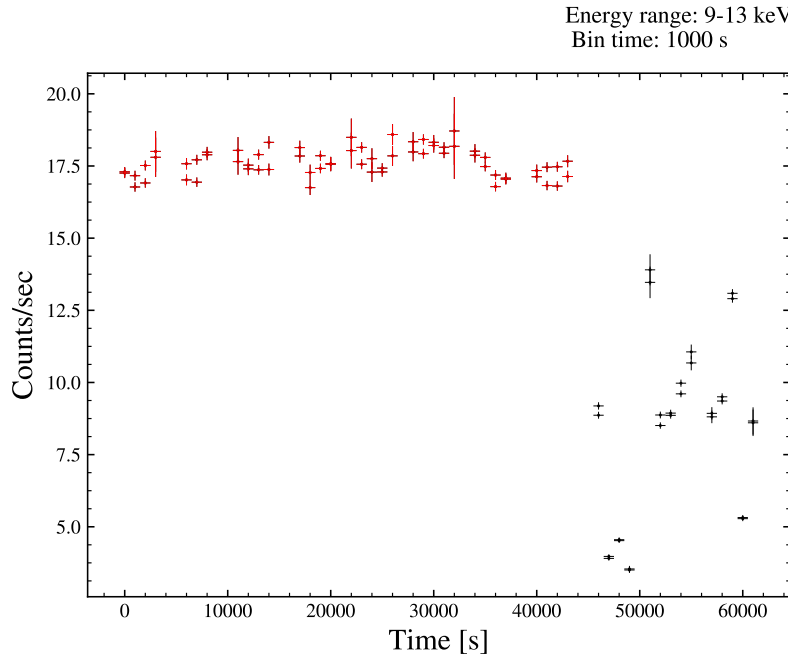


Figure 4.1: Light curve of *NuSTAR* observation with ID 30302012004 in the 9 to 13 keV energy range including a dip. The bin time is 1000 s and the selected data points within a good time interval (GTI) are highlighted in red.

Table 4.1: Summary of the *NuSTAR* observations used for analysis. The observation ID's, start time of observations in MJD and the corresponding date are given, as well as the exposure time (Exp.) and its state. Observations not taking during a main-on are discarded.

Observation ID	MJD start time	Observation date	Exp. [s]	State	Notes
30002006002	56189.700062	Sep 19 2012	28k	Main-on	
30002006005	56192.193200	Sep 22 2012	22k	Main-on	
30002006007	56194.417736	Sep 24 2012	27k	Main-on	
90102002002	57237.703498	Aug 03 2015	22k	Main-on	
90102002004	57241.596709	Aug 07 2015	25k	Off-state	discarded
90102002006	57242.872884	Aug 08 2015	27k	Off-state	discarded
10202002002	57620.207754	Aug 20 2016	37k	Main-on	
30302012002	57970.431043	Aug 05 2016	28k	Main-on	
30302012004	58175.082114	Feb 26 2018	27k	Main-on	
30402009002	58378.844364	Sep 17 2018	28k	Main-on	
30402034002	58523.399661	Feb 09 2019	18k	Main-on	
30402034004	58528.100070	Feb 14 2019	22k	Off-state	discarded
30402034006	58542.257566	Feb 28 2019	23k	Short-on	discarded
30402034008	58556.283736	Mar 14 2019	17k	Main-on	

Table 4.2: Summary of the *HXMT* observations used for analysis. The observation ID's, start time of observations in MJD and the corresponding date are given, as well as the exposure time (Exp.) and its state.

Observation ID	MJD start time	Observation date	Exp. [s]	State
P0101308001	57935.140511	Jul 01 2017	161k	Main-on
P0101308002	57970.286426	Aug 05 2017	87k	Main-on
P0101308003	57971.546264	Aug 06 2017	41k	Main-on
P0101308004	58138.919690	Jan 20 2018	75k	Main-on
P0101308005	58140.178787	Jan 22 2018	167k	Main-on
P0101308006	58175.445882	Feb 26 2018	35k	Main-on
P0101308007	58243.009875	May 05 2018	35k	Main-on
P0101308008	58244.667560	May 06 2018	35k	Main-on
P0101308009	58245.662143	May 07 2018	35k	Main-on
P0101308010	58246.855592	May 08 2018	29k	Main-on
P0101308011	58247.783764	May 09 2018	35k	Main-on
P0101308012	58248.778185	May 10 2018	29k	Off-state
P0101308013	58276.235488	Jun 07 2018	46k	Main-on
P0101308014	58277.560789	Jun 08 2018	35k	Main-on
P0101308015	58278.223416	Jun 09 2018	64k	Main-on
P0101308016	58279.217352	Jun 10 2018	41k	Main-on
P0101308017	58345.046738	Aug 15 2018	18k	Main-on
P0101308018	58345.842085	Aug 15 2018	18k	Main-on
P0101308019	58347.035187	Aug 17 2018	18k	Main-on
P0101308020	58347.830639	Aug 17 2018	18k	Off-state
P0101308021	58349.487930	Aug 19 2018	18k	Main-on
P0101308022	58517.215859	Feb 03 2019	70k	Main-on
P0101308023	58523.453972	Feb 09 2019	29k	Main-on
P0101308024	58527.895442	Feb 13 2019	46k	Off-state
P0101308025	58542.142768	Feb 28 2019	52k	Short-on
P0101308026	58556.198972	Mar 14 2019	52k	Main-on

4.1.2 *HXMT*

Her X-1 was observed by *Insight-HXMT* on numerous occasions between July 2017 and March 2019 (MJD 57935 - 58556). The observation ID's, start and exposure times for each of the three telescopes is listed in Table 4.2.

The data was reduced using the *Insight-HXMT* data analysis software package HXMTDAS v2.01³. Calibrated events were generated from the raw event files using the calibration database CALDB and the HXMTDAS tasks **hepical**, **mepical** and **lepcical** for the HE, ME and LE telescopes, respectively. Good time interval (GTI) files were generated using the **hegtigen**, **megtigen** and **legtigen** tasks and applied to the calibrated events with **hescreen**, **mescreen** and **lescreen**. The data was then barycentrically corrected using the **hxbar** tool and the position of Her X-1 (RA 254.457546 and Dec

³See the data HXMTDAS documentation http://hxmt.org/up1/doc/HXMT_data_reduction_guide_2_01.pdf for a detailed description of the data analysis.

35.342358 , J2000)⁴. Lastly, the binary motion was corrected using the orbital data as reported in Staubert et al. (2009b).

4.2 Data Processing

Once the data was reduced, the goal was to create energy-phase matrices and pulse profiles of all observations. Therefore, the pulse-height amplitude invariant (PI) had to be converted to an energy for both datasets of the *NuSTAR* and *HXMT* observations. This will be described in Section 4.2.1. The exact spin period of the pulsar in Her X-1 is needed for the folding of the events and this calculation is discussed in Section 4.2.2. The event folding and alignment in phase are then explained in Section 4.2.3.

4.2.1 PI to Energy Conversion

The amount of charge that is stored by X-ray detectors is historically called pulse-height amplitude (PHA). PHA cannot directly be converted to energy, as the conversion can vary with time and position on the detector. When this variability is corrected, the result is stored as PI, which is short for PHA invariant. The relationship between PI and the actual energy of the incident photon is encoded in the so-called response file (Arnaud et al. 2011).

The conversion from PI channel to energy is linear for *NuSTAR* observations and the lower energy range of the bin is given by:

$$E = \text{PI} \times 0.04 \text{ keV} + 1.6 \text{ keV}.$$

Similarly, the PI channel was converted to an energy for the *HXMT* detectors according to the response files as follows:

$$\begin{aligned} \text{HE: } E &= \text{PI} \times 370 \text{ keV} \div 256 + 15 \text{ keV} \\ \text{ME: } E &= \text{PI} \times 60 \text{ keV} \div 1024 + 3 \text{ keV} \\ \text{LE: } E &= \text{PI} \times 13 \text{ keV} \div 1536 + 0.1 \text{ keV} \end{aligned}$$

The data of all *NuSTAR* and *HXMT* observations were converted to energies using these conversion formulas.

4.2.2 Spin Period

In order to fold the events of the *NuSTAR* and *HXMT* data, the spin period of each observation has to be determined accurately. The method for this will be explained in the following.

First, the data was categorized in “35 day cycles”. By convention, cycle 0 is the cycle that started around JD 2 441 325.680 (Staubert et al. 1983) and each turn-on defines the start of the next cycle. The cycle numbers for each of the observations from *NuSTAR* and *HXMT* are listed in Tables 4.3 and 4.4, respectively. The spin periods were then determined for each cycle as follows.

⁴<https://heasarc.nasa.gov/cgi-bin/Tools/convcoord/convcoord.pl>

The analysis was conducted using Python 3. `Stingray` is a modern Python library for spectral timing (Huppenkothen et al. 2019) and includes a subpackage called `pulse`. This subpackage contains basic operations to search and characterize pulsed signals, one of which is the Z_n^2 statistics (Buccheri et al. 1983). In contrast to the epoch folding technique, which is another algorithm used to determine pulse periods, the Z_n^2 statistics can distinguish between the correct frequency and its harmonics. The underlying function is given by

$$Z_n^2 = \frac{2}{N} \sum_{k=1}^n \left[\left(\sum_{j=1}^N \cos k\phi_j \right)^2 + \left(\sum_{j=1}^N \sin k\phi_j \right)^2 \right] \quad (4.1)$$

where N is the number of photons, n is the number of harmonics (in the following, $n = 4$) and ϕ_j are the phases corresponding to the arrival times t_j of the photons.

A phase is calculated from the arrival times of the photons, corrected for binary motion, and a trial period. This phase is then entered in Equation (4.1), which returns a value for Z_n^2 . This is repeated for a range of trial periods and the resulting maximum value of Z_n^2 corresponds to the determined spin period. An example of the spin period determination is shown for cycle 457 (*NuSTAR* observation 90102002002) in Figure 4.2.

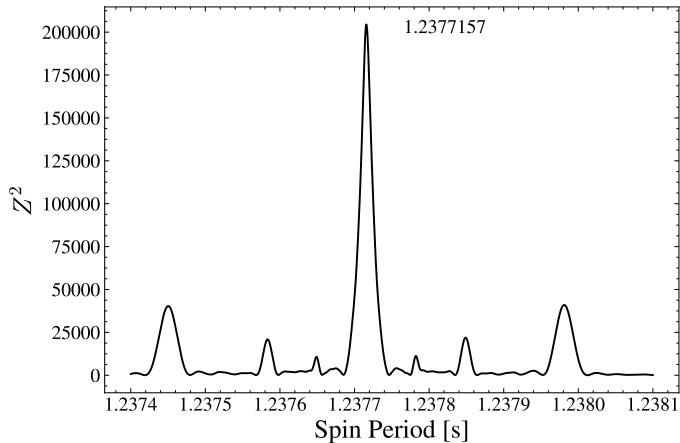


Figure 4.2: An example of the spin period determination (cycle 457, *NuSTAR* observation ID 90102002002) using the Z_n^2 statistics, with $n = 4$.

The data taken by *Insight-HXMT* is split into multiple segments if the observation is longer than one orbit (about 90 minutes). Therefore the segments were merged into a single file for each observation and then the observations for a cycle were combined before the spin period was determined. The spin period of Her X-1 was then determined using the Z_n^2 statistics and the results of the *NuSTAR* and *Insight-HXMT* observations can also be found in Tables 4.3 and 4.4 respectively. These results are roughly consistent with the spin periods of Her X-1 as determined by *Fermi*/GBM⁵.

⁵<https://gammaray.msfc.nasa.gov/gbm/science/pulsars/lightcurves/herx1.html>, accessed on November 19, 2019.

Table 4.3: Cycle numbers and relative spin periods of the *NuSTAR* observations used for the analysis.

Cycle	Observation ID	Spin Period [s]
427	3000200600X: 2, 5, 7	1.2377191
457	90102002002	1.2377157
468	10202002002	1.2377169
478	30302012002	1.2377181
484	30302012004	1.2377197
490	30402009002	1.2377175
494	30402034002	1.2377162
495	30402034008	1.2377184

Table 4.4: Cycle numbers and relative spin periods of the *HXMT* observations used for the analysis.

Cycle	Obs ID	Spin Period [s]
P01013080XX		
477	01	1.2377174
478	02, 03	1.2377175
483	04, 05	1.2377166
484	06	1.2377197
486	07, 08, 09, 10, 11, 12	1.2377196
487	13, 14, 15, 16	1.2377208
489	17, 18, 19, 20, 21	1.2377103
494	22, 23, 24, 25	1.2377178
495	26	1.2377180

4.2.3 Event folding

After the determination of the spin period, the events were folded using the `stingray` function `fold_events`, which uses as parameters the (binary corrected) arrival times of the photons, the spin period, calculated in Section 4.2.2, and the number of bins in the pulse profile. For the following analysis, 128 phase bins were chosen. The event folding function returns three arrays: the phase bins, the pulse profile and the uncertainties of this pulse profile.

In order to compare pulse profiles of different observations and instruments, the pulse profiles need to be aligned in phase. To do this, the “sharp edge” feature was used, as described in Staubert et al. (2009a,b). This feature is at the right edge of the main peak, as shown in Figure 2.8, and it is the sharpest and most stable feature of the pulse profiles. The sharp edge can be described by a “more steep” or “less steep” edge:

$$\begin{aligned} \text{less steep: } f(\phi) &= -799.38 \times \phi + 803.26 \\ \text{more steep: } f(\phi) &= -1398.90 \times \phi + 1386.41 \end{aligned}$$

for a phase $\phi \in [0.93, 1.00]$. The sharp edges can be seen in Figure 4.3 in comparison with the *RXTE* template profiles (introduced in Section 2.2.2).

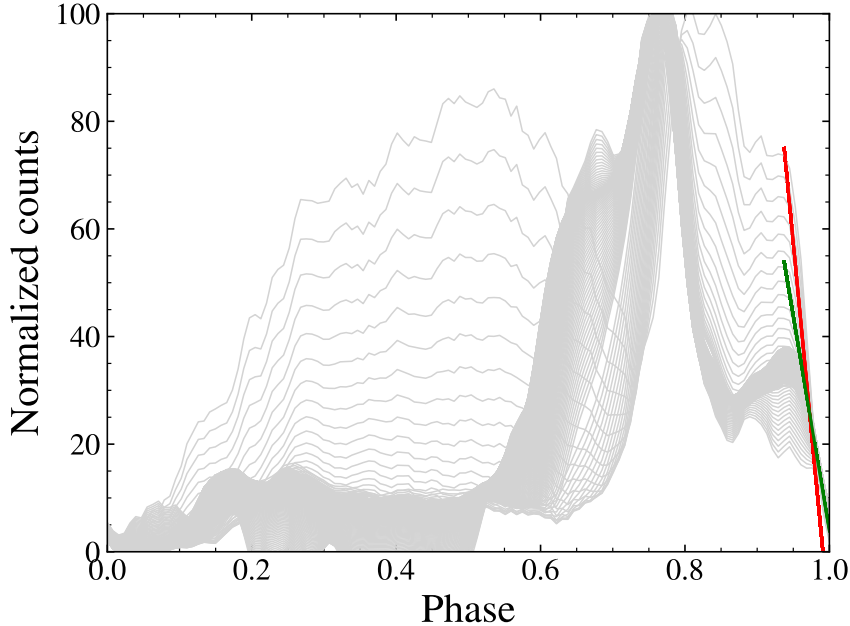


Figure 4.3: Definition of the sharp edges (more steep in red, less steep in green) in comparison with the *RXTE* template for comparison.

The *NuSTAR* data was binned for an energy range of 9 to 13 keV and the resulting pulse profiles were smoothed by taking a running mean of three consecutive phase bins and normalized between 0 and 100. Then, they were compared with the edges using a χ^2 test and a range of phase shifts $\Delta\phi$. The dataset was then shifted in phase by the $\Delta\phi$ which corresponded to the minimum χ^2 value. The *HXMT* data was binned for each telescope as follows:

- HE: 13 to 51 keV
- ME: 9 to 13 keV
- LE: 0.1 to 11.1 keV

and the same procedure as for *NuSTAR* was applied to align the pulse profiles in phase. The energy ranges of the HE and LE telescopes were chosen as close to the 9 to 13 keV energy range as possible.

With this data, the further analysis can be conducted and energy-phase matrices, as well as pulse profiles can be created, as described in Section 4.3.

4.3 Results

In this section, the results of the data analysis are presented. A description of the energy-phase matrices is given in Section 4.3.1, followed by the pulse profiles in Section 4.3.2 and a discussion of the pulse profile fitting in Section 4.3.3. Since this analysis contains a “mass production” of different plots (more than 300 plots, cf. Section 1.1), only a few exemplary figures are presented here. All plots can be found under

https://gitlab.com/isaathoff/master_thesis_results.

4.3.1 Energy-Phase Matrices

Energy-phase matrices can be created where the phase bins are on the x-axis, the energy is on the y-axis and the number of photons are color coded. The *NuSTAR* and *HXMT* data were also divided into time-bins of 10 000 s and 20 000 s, respectively, and the resulting matrices will be presented in the following.

Matrices based on *NuSTAR* data

The results for the *NuSTAR* data are shown exemplary in Figure 4.4 for observation 30002006005 of cycle 427. The four panels each show 10 000 s of data.

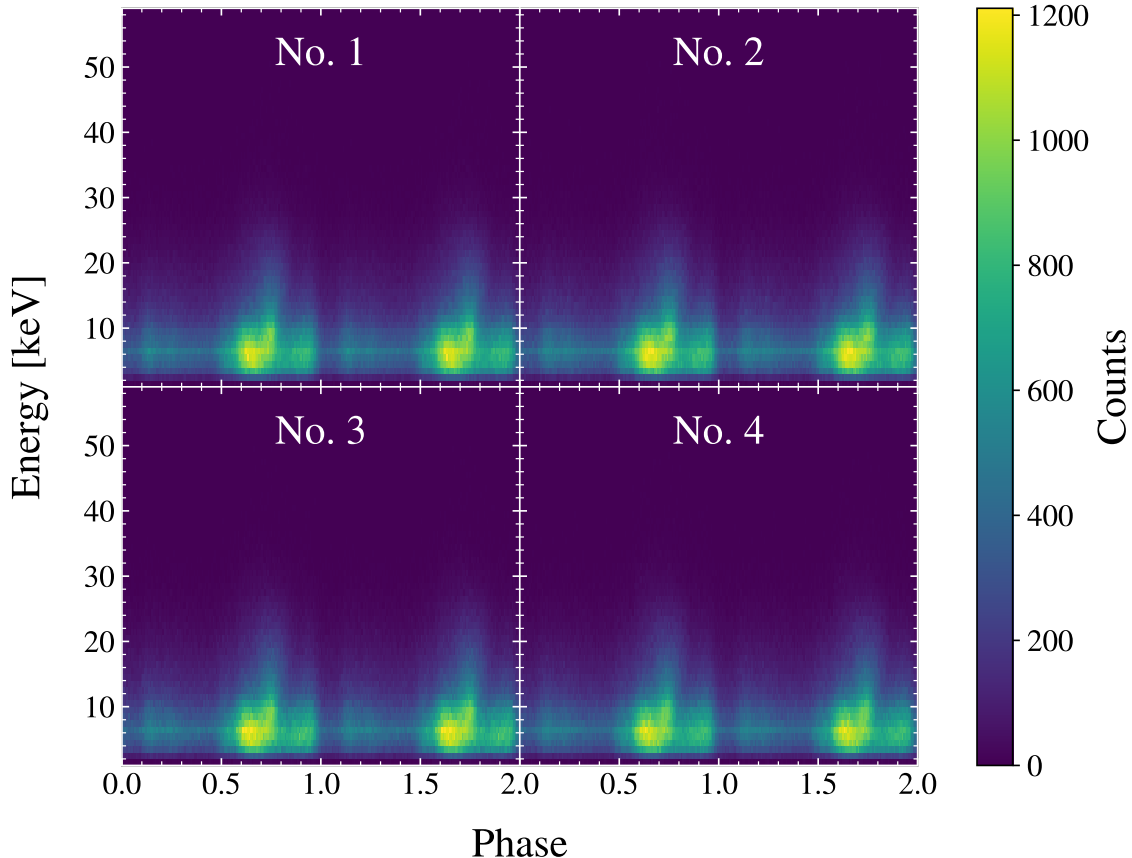


Figure 4.4: Example matrix of the *NuSTAR* observation 30002006005, cycle 427. Each panel (No. 1 – 4) shows 10 000 s of data.

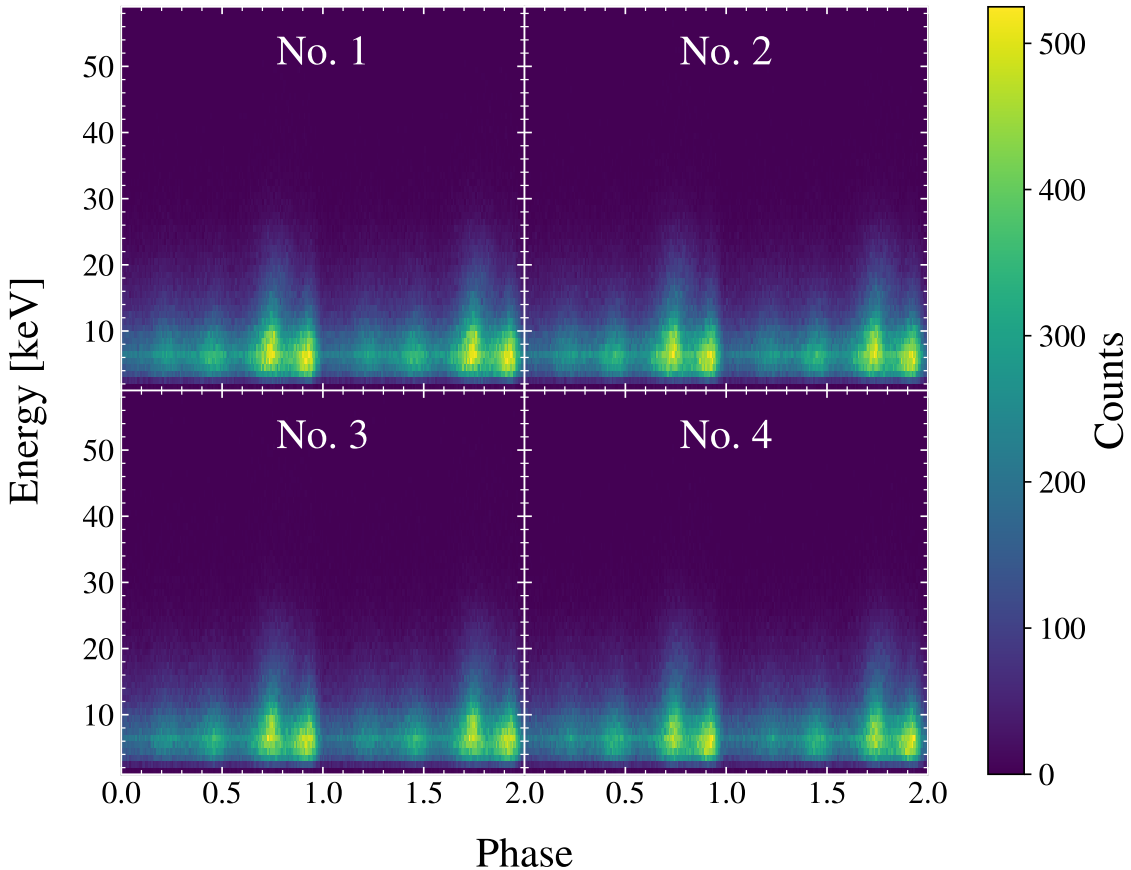


Figure 4.5: Matrix of the *NuSTAR* observation 90102002002, cycle 457, every 10 000 s. Four bright spots can be seen.

The matrices of cycles 427, 468, 490 and 494 show, as expected, a faint interpulse and, more clearly, the main pulse. Above 30 keV the counts detected drop well below 200 and therefore no structures can be distinguished at higher energies. The majority of the counts was detected below 10 keV. A time dependence within each cycle is not observed.

The matrices of cycles 457, 478, 484 and 495 show an unexpected pattern as two very bright spots and two fainter spots can be made out. An example of this can be seen for cycle 457 in Figure 4.5. For a further analysis, however, I refer to the next section, which is dealing with the pulse profiles generated from these matrices.

Matrices based on **HXMT** data

Similarly, an example of the HXMT results is shown in Figure 4.6. In the bottom panel, the matrix for the LE telescope is shown for an energy range of 1 to 12 keV. The interpulse and main pulse can be seen and most counts were clearly detected at around 2 to 4 keV. The middle panel shows the ME telescope and the two pulses can also be distinguished quite clearly. The results of the HE telescope is shown in the top panel, where virtually no photons were detected below 45 keV and above 60 keV and in-between the main pulse clearly dominates.

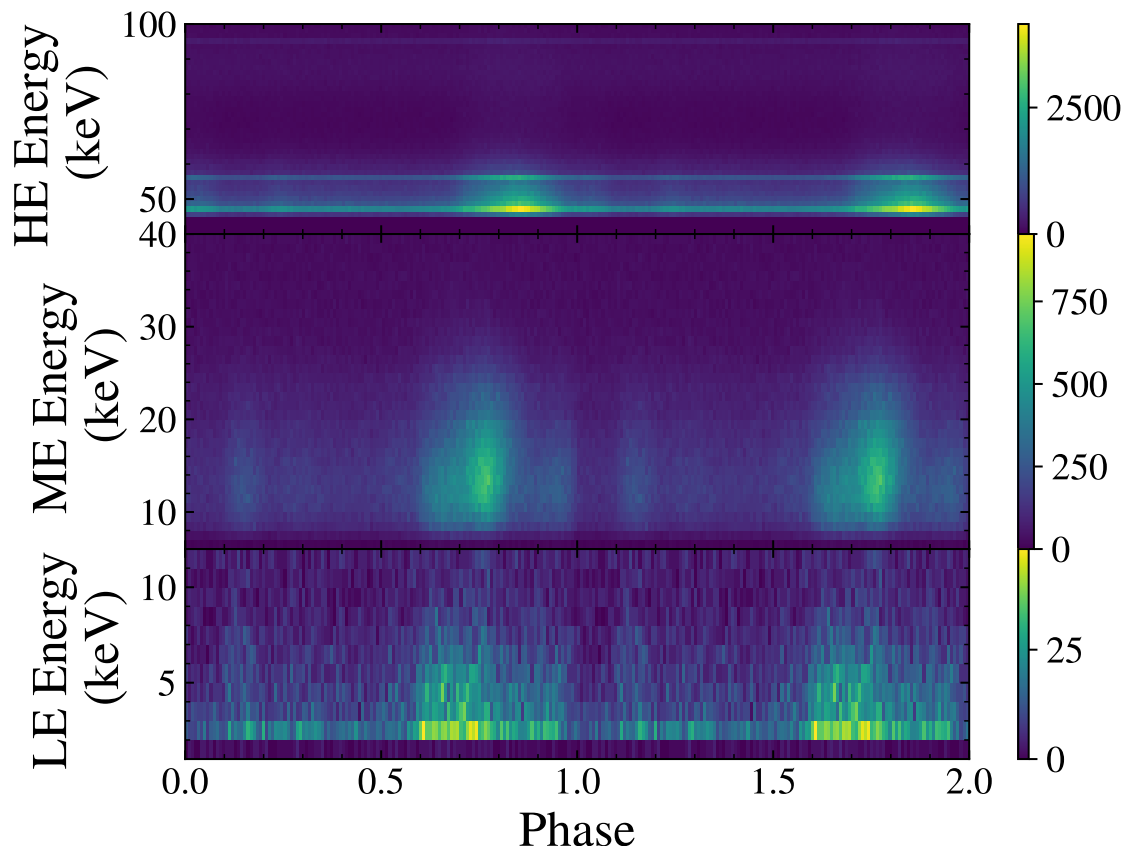


Figure 4.6: Profile matrix of *HXMT* observation P0101308001, cycle 477, segment 1, the first 20 000 s.

4.3.2 Pulse Profiles

By reading out the matrices horizontally and binning the energies, pulse profiles can be created. For both *NuSTAR* and *HXMT*, the energy ranges that were chosen can be found in Table 4.5.

Table 4.5: Energy bins for the pulse profiles of the *NuSTAR* and *HXMT* data.

<i>NuSTAR</i>	<i>HXMT</i>
3 to 4.5 keV	LE: 0.1 to 11.1 keV
4.5 to 5.5 keV	ME: 3 to 9 keV
6.5 to 9 keV	ME: 9 to 13 keV
9 to 13 keV	ME: 13 to 63 keV
13 to 19 keV	HE: 42 to 51 keV
19 to 33 keV	HE: 51 to 73 keV
33 to 78 keV	HE: 73 to 113 keV

Pulse Profiles based on *NuSTAR* data

An example of the pulse profiles based on *NuSTAR* data, the first 10 000 s of cycle 468 with observation ID 10202002002, can be seen on the left side of Figure 4.7. In the 9 to 13 keV energy range, the main features can be seen as introduced in Section 2.2.2 and Figure 2.8. The interpulse and main pulse with its leading and trailing shoulders is distinguishable and the pre-interpulse minimum is clearly visible. Moving from this toward lower energies, both the leading and trailing shoulders increase and the leading shoulder starts to dominate even the hard central peak. The sharp edge becomes slightly steeper but there is little change in the pre-interpulse minimum and the interpulse itself. Moving from 9 to 13 keV to higher energies, the trailing shoulder decreases but is still visible, while the leading shoulder merges into the hard central peak and becomes undistinguishable. The interpulse also decreases in intensity and the sharp edge becomes much less steep. In the profile above 33 keV the features are not recognizable any more due to low statistics. The pulse profiles of observations during cycles 427, 468, 490 and 494 all show profiles similar to the example and the general description.

In a few pulse profiles, those from cycles 457, 478, 484 and 495, new features have been observed. An example can be seen on the right side of Figure 4.7. Starting again with the 9 to 13 keV energy range, the differences can immediately be seen. The hard central peak can still be distinguished, but there appears to be no leading shoulder. The trailing shoulder on the other hand is a lot more defined and the profile therefore appears double-peaked. Due to this, the sharp edge is also more distinct and steeper. The pre-interpulse minimum is not as clear but the interpulse can still be seen. Another new feature is a previously not observed peak between the interpulse and the main peak. It is unclear, if this peak has originated and transitioned from the leading shoulder or if it is a completely new feature. When moving to lower energies, the trailing shoulder starts to exceed the hard central peak, which has also not been observed before, and the central peak becomes less defined. The new peak between interpulse and main pulse increases, which would support the theory that it has evolved

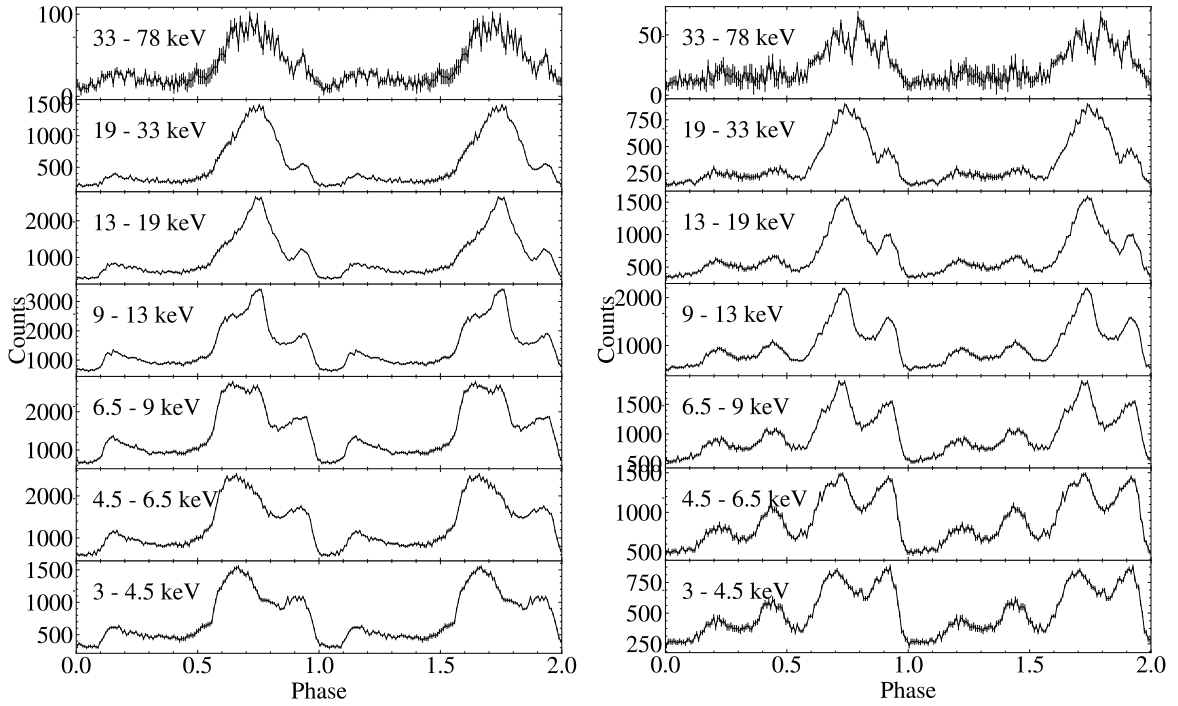


Figure 4.7: Pulse profile of the first 10 000 s of *NuSTAR* observation 10202002002 (cycle 468) on the left and 30302012002 (cycle 478) on the right.

from the leading shoulder. However, at these lower energies, especially between 6.5 to 9 keV, a leading shoulder is indicated in addition to the new peak. When comparing higher energies to the 9 to 13 keV energy range, the trailing shoulder decreases in energy and the sharp edge becomes less steep again. The interpulse and new peak between the interpulse and main pulse appear to merge and become indistinguishable. Again, the low statistics above 33 keV make any features indistinct.

Pulse Profiles based on *HXMT* data

Figure 4.8 shows exemplary 20 000 s of *HXMT* observations during cycles 487 (left side of the figure) and 484 (right side of the figure). The top three panels (blue, energy ranges 13 to 51 keV, 51 to 73 keV and 73 to 113 keV) are data taken with the HE telescope, the subjacent three panels (yellow, energy ranges 3 to 9 keV, 9 to 13 keV and 13 to 63 keV) show ME data and the bottom panel is based on the LE telescope data (red, energy range 0.1 to 11 keV).

Cycles 477, 483, 486, 487, 489 and 494 show the same general profile as the example from Section 2.2.2 (Figure 2.8) but in cycles 478, 484 and 495 the four-peaked structure that was already observed in cycles 457, 478, 484 and 495 of the *NuSTAR* data, is again observed.

A direct comparison of data from *NuSTAR* and *HXMT* during the same cycles (478, 484, 494 and 495) is given in the next subsection.

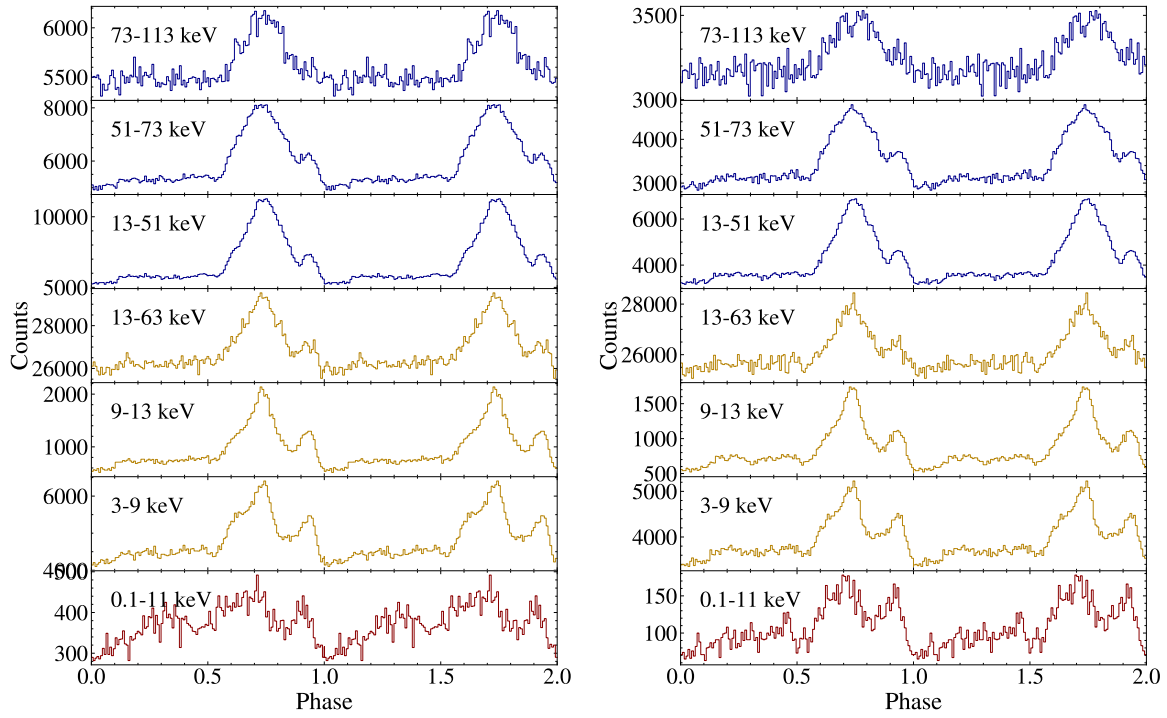


Figure 4.8: Pulse profile of the first 20 000 s of *HXMT* observation P0101308014 (cycle 487) on the left and P0101308006 (cycle 484) on the right.

Direct Comparison of *NuSTAR* and *HXMT* Data

During cycles 478, 484, 494 and 495, both *NuSTAR* and *HXMT* observed Her X-1. In order to make a direct comparison of the two data sets, the energy ranges for the pulse profiles were adjusted as follows: 1 to 9 keV, 9 to 13 keV, 13 to 20 keV, 20 to 30 keV and 30 to 58 keV.

These energy ranges are covered completely by *NuSTAR* and *HXMT*. The lowest energy range was covered by the LE telescope on *HXMT* and the highest energy range by the HE telescope. Data from the ME instrument was used for the remaining three ranges.

The data was then smoothed by taking a running mean of three adjacent phase bins, and normalized between 0 and 100 in order to make a direct comparison possible. In Figures 4.9 and 4.10 one example is shown for each cycle. The right panel shows results for (*HXMT-NuSTAR*). The green and blue vertical color bars serve to guide the eye and cover in the three adjacent panels (*HXMT*, *NuSTAR* and *HXMT-NuSTAR*) the same phase ranges.

Since the 1 to 9 keV and 30 to 58 keV show poor statistics in the *HXMT* and *NuSTAR* data, respectively, these panels will be omitted in the following descriptions.

Cycles 478, 484 and 495 appear similar, each showing slight variations between the data sets. It appears that the *NuSTAR* profiles generally show wider peaks. Between phases 0.6 – 0.7, *HXMT* shows fewer counts and in the subsequent phases 0.7 – 0.8 it tends to show more counts. The general shape of the profiles is the same and the four peaked structure and sharp edges can be seen in all profiles similarly.

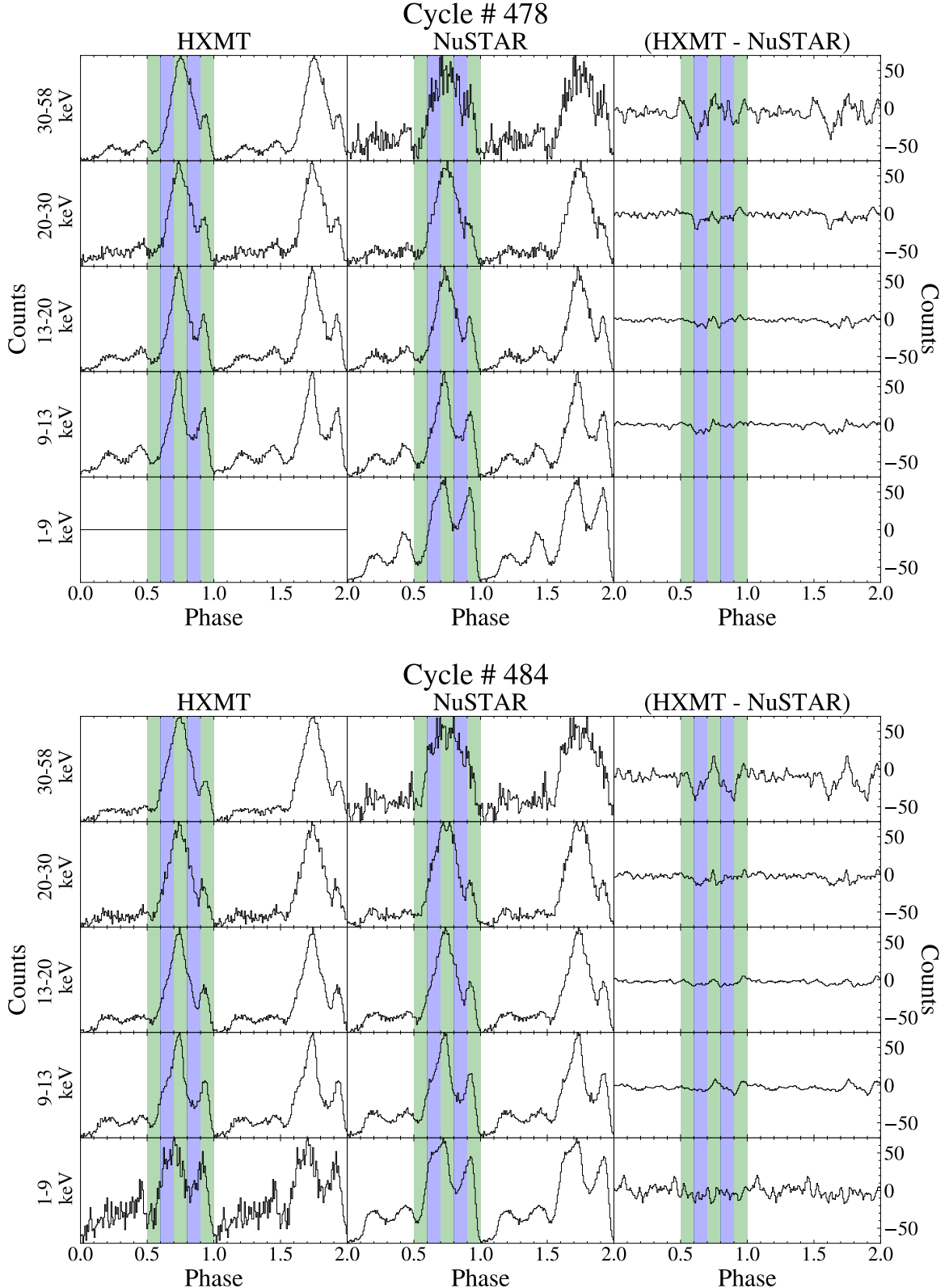


Figure 4.9: Comparison of *HXMT* (left panel) and *NuSTAR* (middle panel) pulse profiles of cycles 478 and 484. The last panel shows the difference between the smoothed and normalized profiles of *HXMT* and *NuSTAR*. The vertical color bars are to guide the eye.

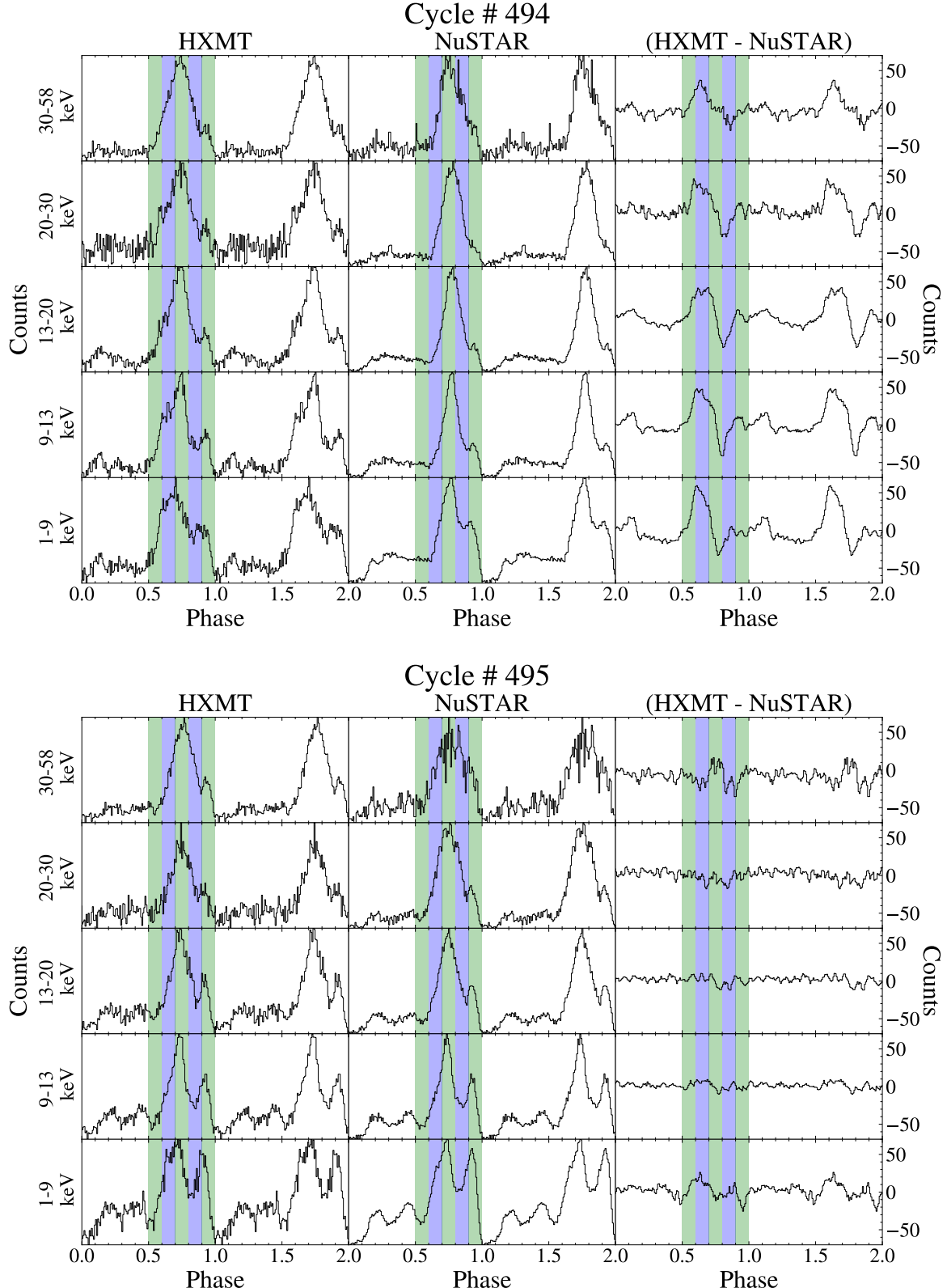


Figure 4.10: Comparison of *HXMT* (left panel) and *NuSTAR* (middle panel) pulse profiles of cycles 494 and 495. The last panel shows the difference between the smoothed and normalized profiles of *HXMT* and *NuSTAR*. The vertical color bars are to guide the eye.

Table 4.6: Comparison of the spin periods as determined from the *NuSTAR* and *HXMT* data for cycles 478, 484, 494 and 495.

Cycle	Spin Period [s]	Spin Period [s]	Difference [s]
	<i>NuSTAR</i>	<i>HXMT</i>	
478	1.2377181	1.2377175	6×10^{-7}
484	1.2377197	1.2377197	0
494	1.2377162	1.2377178	1.6×10^{-6}
495	1.2377184	1.2377180	4×10^{-7}

The largest differences can be seen in cycle 494 where the shape of the profiles differs. Especially in the 9 to 13 keV energy range, the *HXMT* profile shows a strong shoulder on the left side of the main pulse and the shoulder on the right side is very dominant. The *NuSTAR* data of the same cycle looks very different, as no shoulder can be seen on the left side and the shoulder on the right side is less pronounced. These differences manifest itself in the third panel, where a systematic difference of the counts can be seen.

These differences are probably due to the different spin periods that were determined for the cycles between the datasets, see Table 4.6. Another difference could be caused by the time intervals chosen, which were 10 000 s for *NuSTAR* and 20 000 s for *HXMT*. The largest difference was found, as expected from the top of Figure 4.10, for cycle 494.

4.3.3 Pulse Profile Fitting and (O-C) diagram

The goal of this part of the work is to determine the turn-on of the super-orbital (~ 35 d) cycle by pulse profile fitting as described in Section 2.2.2 and compare this to the observed turn-on times from the light curve in an updated (O-C) diagram (see Figure 2.11). In the following, C will describe the calculated turn-on time, using a period of 34.85 d and a reference time at 42409.943 MJD; the observed turn-on times from the light curve will be dubbed O^{LC} and the turn-on times as derived from the pulse profile fitting method will be referred to as O^{PP} . The O^{LC} data is based on *Swift*/BAT data in the 15 keV to 50 keV energy range and was provided by R. Staubert (private communication 2019).

Since the observations done with *NuSTAR* and *HXMT* are too short to create new pulse profile templates, the template of *RXTE* observations from 1996 to 2005, described in Section 2.2.2 was used to determine the phases of the observations. As can be seen in Figure 2.12, the *RXTE* template is not precisely normalized between 0 and 100 as some profiles have values below zero, some appear to be cut off at zero, some do not seem to reach 100 counts at their maxima and some exceed it. It is believed, however, that this is negligible for the overall shape of the pulse profiles and therefore of no further consequence for the determination of the super-orbital phase.

The template covers an energy range of 9 to 13 keV and therefore the same energy range was extracted of the *NuSTAR* and *HXMT* data (see the corresponding pulse profiles for example in Figures 4.7 and 4.8). The data was first smoothed by taking a running mean of three adjacent phase bins and subsequently normalized between 0 and 100 counts to correspond with the *RXTE* template profiles. Then, the data was compared to the template profiles using a χ^2 test and the minimal χ^2 value was indicative of the best fit. Two examples can be seen in Figure 4.11 where the data (in this case *NuSTAR* observation 10202002002 on the left and 30302012002 on the right) is shown in blue, the entire *RXTE* template can be seen in light gray and the best fitting profile of the template is highlighted in orange. In these examples the best fitting profiles correspond to a 35 day phases of 0.0920 and 0.1840, respectively.

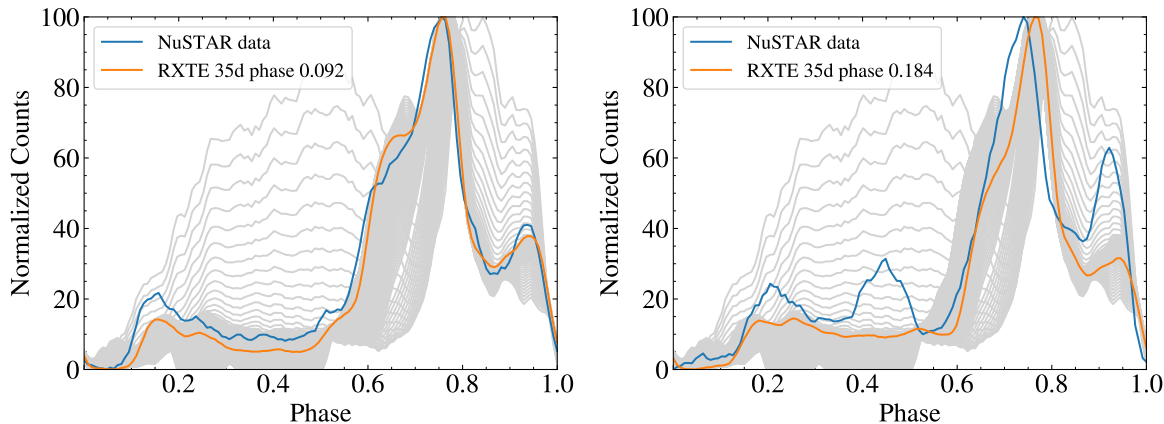


Figure 4.11: Template fitting, exemplary for the first 10 000 s of *NuSTAR* observations 10202002002 (left) and 30302012002 (right). The smoothed and normalized data is shown in blue and the entire *RXTE* template is displayed in light gray. The best fitting profile of the template is highlighted in orange.

This procedure was repeated for all observations. The determined 35 day phases can be found in the appendix, Tables 1 and 2 for *NuSTAR* and *HXMT* data, respectively. Since the *RXTE* template appears erratic for phases over 0.2, results with a phase above 0.2 were discarded. The uncertainties of these phases were estimated as follows: the phases determined from pulse profile fitting (ϕ^{PP}) were subtracted from the phases that were calculated from the observed turn-on of the light curve (ϕ^{LC}). The distribution ideally has a mean value of zero. For *NuSTAR*, the mean value is at a phase of -0.009 with a one sigma width of 0.027. The *HXMT* data shows a mean value of 0.005 and a one sigma width of 0.036. Therefore, the total uncertainty, which is the combined systematic and statistical uncertainties, is assumed to be 0.03 and 0.04 for *NuSTAR* and *HXMT*, respectively.

Determination of the Turn-On Time with a 34.85 d Model

As introduced in Section 2.2.2 and shown in Figure 2.13, Staubert et al. (2013) propose to take the weighted mean of all values within a 35 day cycle and extrapolating using a cycle length of 34.85 d to get the zero phase, which corresponds to the turn-on time, O^{PP} , of the cycle. Following this approach, the results of the *NuSTAR* and *HXMT* data is visualized in Figures 4.12 and 4.13, respectively. Note that these plots only serve as a visualization and the data was not fitted.

By looking at this data, several questions arise:

- It is not clear if the pulse profiles change systematically with 34.85 d. This is especially evident in cycle 478. The determined phases do not appear to show any clear trend, both in *NuSTAR* and *HXMT* data. Does the pulse profile really change regularly with the 34.85 d cycle?
- What is the significance of the results, when only one or two phase points could be extracted during one particular cycle?
- The one sigma uncertainty intervals of 0.03 and 0.04 span over 30 - 40 % of the accessible 35 day phase range covered by the template. What does this say about the reliability of the method?

These questions will be addressed in more detail in the following sections. First however, for completeness, the results using the model with a cycle length of 34.85 d will be presented. The in-depth analysis of the method itself will be discussed in the subsequent sections.

The turn-on times, O^{PP} , have been determined using the model of 34.85 d and the resulting (O-C) diagram can be seen in Figure 4.14. The uncertainties were calculated from the corresponding uncertainties of the 35 day phases:

$$\begin{aligned} \textit{NuSTAR}: \Delta(O^{\text{PP}} - C) &= 0.03 \times 34.85 \text{ d} = 1.05 \text{ d} \\ \textit{HXMT}: \Delta(O^{\text{PP}} - C) &= 0.04 \times 34.85 \text{ d} = 1.39 \text{ d} \end{aligned}$$

The uncertainties of the turn-on times, O^{PP} , determined in the present analysis are a lot larger than the previously determined data (Staubert et al. 2013). Nonetheless, the turn-on times from pulse profile fitting seem to track the turn-on times from the light curve very well. However, this might be due to the nature of the method, which will be discussed in the following section.

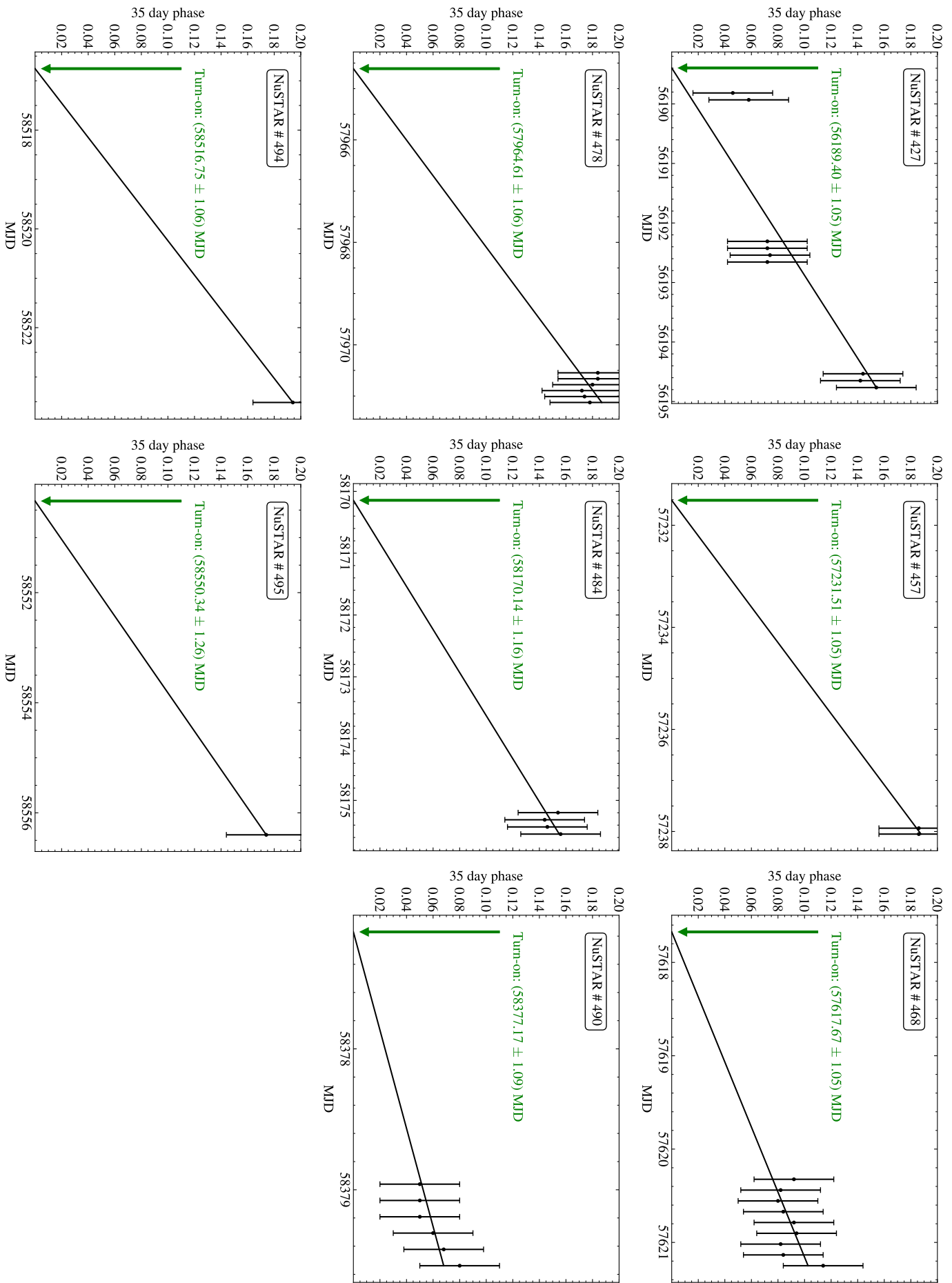


Figure 4.12: Determination of the phase zero/turn-on time based on pulse profile fitting (OPP) on the basis of *MuSTAR* data.

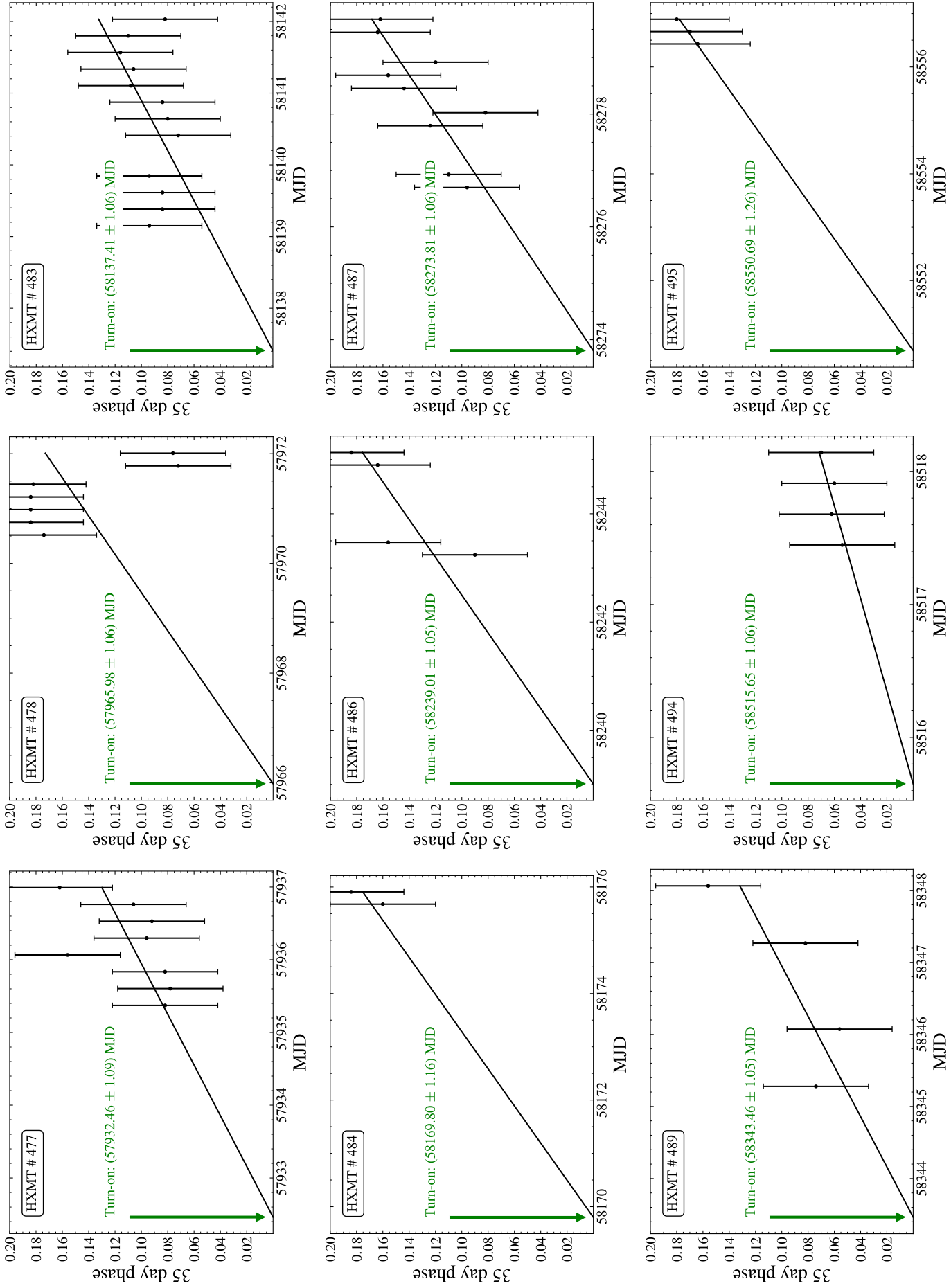


Figure 4.13: Determination of the phase zero/turn-on time based on pulse profile fitting (O^{PP}) on the basis of *HXMT* data.

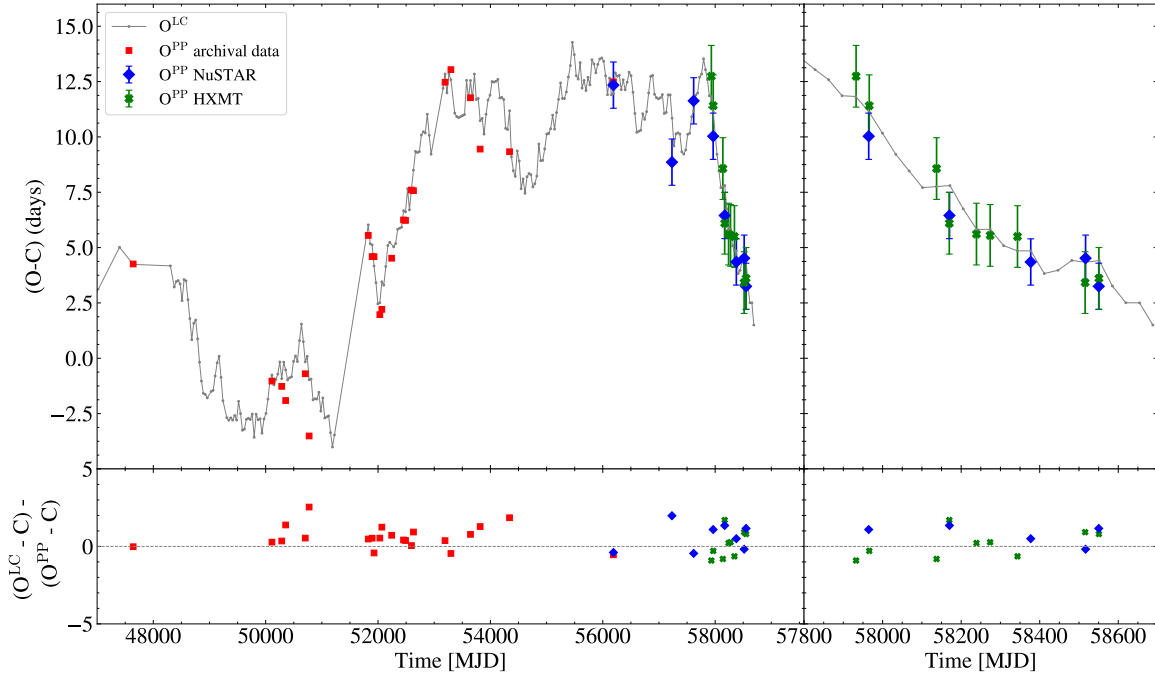


Figure 4.14: Updated (O-C) diagram. The $(O^{LC}-C)$ data is shown in gray, the $(O^{PP}-C)$ data from Staubert et al. (2013) is displayed in red squares, the *NuSTAR* data in blue diamonds and the *HXMT* as green crosses. The right panel shows a zoom-in to the last 800 days and the bottom panels shows the residuals.

4.3.4 Analysis of the Pulse Profile Fitting Method

Staubert et al. (2009a) proposed that during the anomalous low in 1999, the NS free precession and the precession of the accretion disk somehow lost their synchronization. Since then Staubert et al. (2013) have designed a method to test the opposing idea: that the pulse profile evolution (caused by a free precession of the NS) and the turn-on observed from the light curve (caused by the precession of the accretion disk) are indeed caused by the same “clock”. To prove this, two different (O-C) diagrams were created, one based on the light curve data, using O^{LC} , and one using the pulse profile fitting method and the derived O^{PP} . Therefore, as already mentioned in the previous section, three components are needed:

1. C: the calculated turn-on time, based on a zero time and an essentially arbitrary cycle length (generally assumed to be the mean cycle length of 34.85 d);
2. O^{LC} : the observed turn-on time, based on the observed flux variations in the light curve, O^{LC} is defined as the time where the X-ray flux reaches 10% of the maximum flux of its corresponding main-on;
3. O^{PP} : the observed turn-on time, based on the pulse profile fitting method.

The calculated turn-on time serves only as a reference time, whereas O^{LC} and O^{PP} are based on observations. Using components 1. and 2., the $(O^{LC}-C)$ can be created, as shown in the top left panel of Figure 4.15.

If the period of 34.85 d were stable, this curve would be a constant at $(O-C) = 0$. The observed variations show that the super-orbital period is not constant, but varies

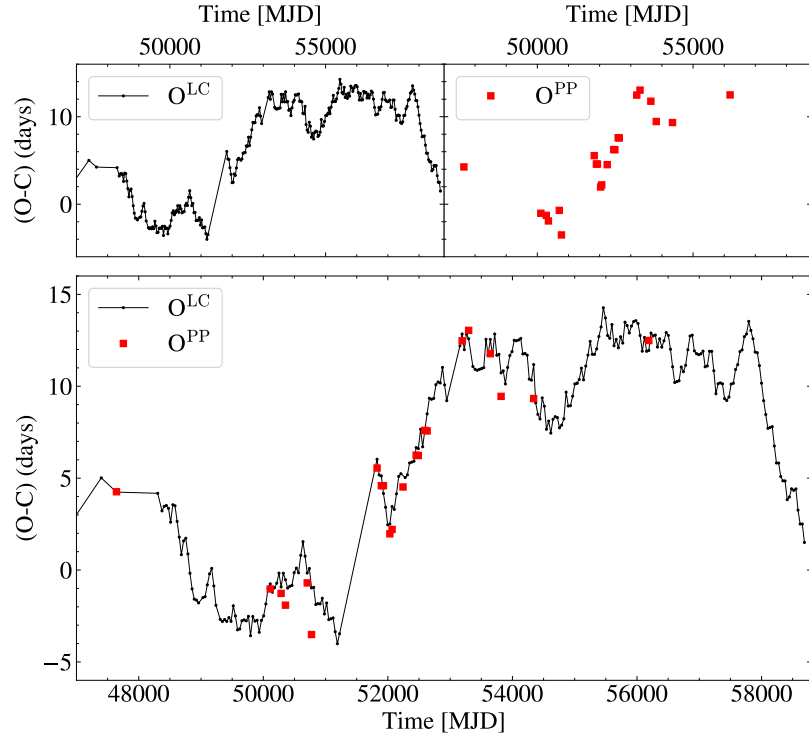


Figure 4.15: The separate (O^{LC} -C) (top left) and (O^{PP} -C) (top right) diagrams, as well as the combined diagram (bottom panel). (Data from R. Staubert, private communication 2019.)

slightly with time. This result is solely based on the observation of the light curve of Her X-1 and it is assumed to be due to the precession of the accretion disk (Staubert et al. 2013).

Assuming that the pulse profile evolves systematically during the super-orbital cycle, the turn-on time can be inferred using an entirely independent method, using components 1. and 3. The (O^{PP} -C) diagram can then be created, see the top right panel of Figure 4.15, which is entirely independent of the previously determined (O^{LC} -C) diagram as it is based on a different type of observation. The pulse profile is thought to change due to some variation closer to the NS itself, e.g. a free precession (Staubert et al. 2009a).

Only in a last step, by comparing the two diagrams (O^{LC} -C) and (O^{PP} -C), see the bottom panel of Figure 4.15, are the two methods compared and it can be concluded if the small changes in the period are due to the same physical process or if indeed two clocks are present in the system.

The procedure of how to determine O^{PP} is, however, central: by comparing the observations with the pulse profile template, phases are determined for each observation as described above. If the pulse profile changes regularly during the super-orbital cycle, the “35 d Phase vs. MJD” plots (Figures 4.12 and 4.13) would be expected to show this trend. The 35 d phase would change with time as

$$\frac{d\phi}{dt} = \frac{1}{34.85} \left[\frac{1}{\text{MJD}} \right]. \quad (4.2)$$

Thus far, however, it has not been tested if this model is represented by the data, but only assumed for the determination of O^{PP} . Similarly as the determination of O^{LC}

relies only on observations, O^{PP} should also be solely based on observations and not assume a model of 34.85 d, as it has not been tested yet if the pulse profile changes reasonably regular with the super-orbital phase.

It is unclear at this point, if assuming a model of a 34.85 d cycle in the O^{PP} determination leads to a circular conclusion. Regardless of this, the model needs to be tested and it needs to be confirmed that it is reasonable to assume a constant cycle length of exactly 34.85 d for the evolution of the pulse profiles. In the following, this will be discussed in more detail.

The above mentioned questions in Section 4.3.3 from the observations of the 35 d phase based on pulse profile fitting will now be analyzed in-depth. To recapitulate, the findings of these observations are:

- Thus far, the assumption was that the pulse profile evolution is regular with super-orbital phase and therefore the phase of the system can be accurately determined purely based on the pulse profiles. Especially cycle 478 of both *HXMT* and *NuSTAR* data does not seem to show any clear trend. By combining the observations, see Figure 4.16, it appears to be either flat or even decrease with time, as opposed to the generally observed and assumed increase.

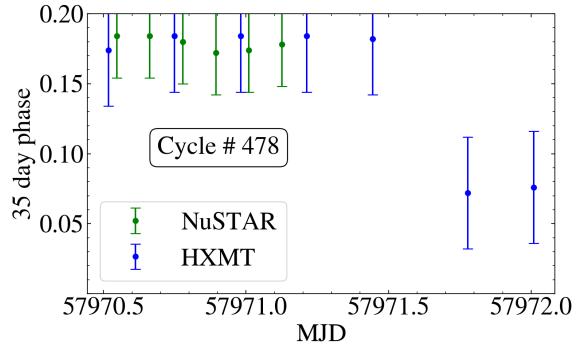


Figure 4.16: 35 d phases of cycle 478 from both *NuSTAR* (green) and *HXMT* (blue) data.

- The range of the pulse profile template of 0 to 0.2 in 35 day phase is very small and the one sigma uncertainty interval of the phases determined by the pulse profile fitting is comparably large: 0.03 - 0.04 spans over 30 - 40 % of the accessible range.

In order to analyze these observations in more depth, the following points were examined:

A: Linear Regression. To get a better understanding of the first point - that the pulse profile evolution does not appear to change as regularly with 34.85 d as assumed - a trial was conducted using the *RXTE* data of cycle 257 from Staubert et al. (2013). The data was fit without the model of a 34.85 d cycle. Figure 4.17 shows the same data from the paper (see also Figure 2.13) and the magenta line shows the solution using a weighted average and an extrapolation using a 34.85 d period to infer the phase zero and therefore the turn-on time of the cycle. This yielded approximately the same turn-on time as reported by Staubert et al. (2013). The black line show a

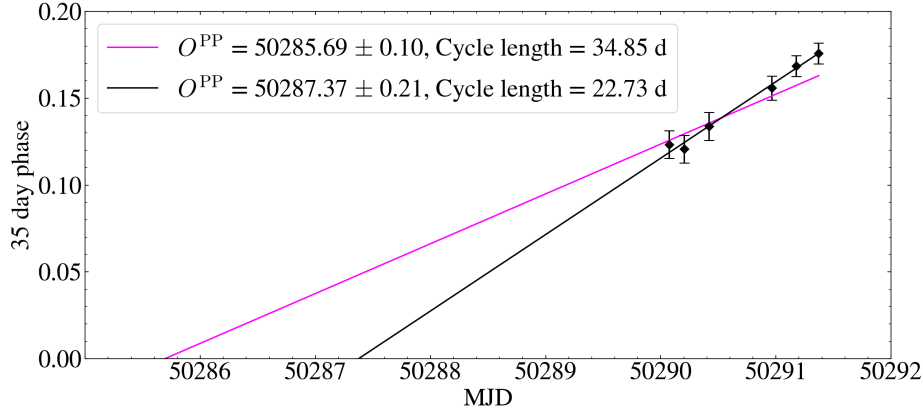


Figure 4.17: Zero phase determination based on pulse profile fitting data using a fixed slope of 34.85 d (magenta) and using a fit with a free slope parameter (black). The data points are taken from Staubert et al. (2013), cycle 257 with *RXTE* data.

linear regression. Here, the cycle length is not fixed to a particular value, which leads to a drastically shorter cycle length of only about 23 d and a turn-on time based on pulse profile fitting of $O^{PP} \approx (50287.4 \pm 0.2)$ MJD.

Since this data does not seem to follow the model that the pulse profile evolves regularly with a period of 34.85 d, the *NuSTAR* and *HXMT* data was reanalyzed and the phases from Figures 4.12 and 4.13 were fit using a linear regression where the slope is kept as a free parameter. Cycles with only 1-2 data points were removed from the sample as a linear regression would be meaningless in these cases. The remaining cycles and corresponding fits can be seen in Figures 4.18 and 4.19.

Based on these fits, a cycle length could be inferred from the slope (see also Equation (4.2)). These results can be seen in Table 4.7. The determined cycle lengths range from about 10 d to 150 d. Since it is physically unreasonable to assume that the cycle length varies by large factors as these within a few cycles, this might be an indication of a possible shortcoming in the pulse profile fitting method.

For completeness, the turn-on times determined by calculating the zero phase are shown in Tables 4.8 and 4.9 and are also displayed in an (O-C) diagram in Figure 4.20. The uncertainties are much larger and the points do not follow the data from the light curve as closely as before, however, the general trend can still be seen.

Cycle 478 presents a special case, the data of both *NuSTAR* and *HXMT* was already shown in Figure 4.16. The determined 35 d phases are decreasing instead of increasing over time, opposite to the expected evolution. Therefore these data could also not be used to determine a phase zero/turn-on time using this method and were discarded in the following. A reason for this could be the four-peaked structure of the pulse profiles, which might lead to a wrong determination of the phase during the fitting procedure with the *RXTE* pulse profile template, that were discussed in Section 4.3.2. However, cycles 484 and 495 also displayed the four-peaked structure and the results of these cycles are as expected compared to the light curve data. Therefore, it is not yet clear why cycle 478 presents such a special case.

The results for the calculated turn-on, C, the observed turn-ons based on the light curve, O^{LC} , and the turn-ons based on pulse profile fitting, O^{PP} , can be seen in Tables 4.8 and 4.9 for the *NuSTAR* and *HXMT* observations, respectively.

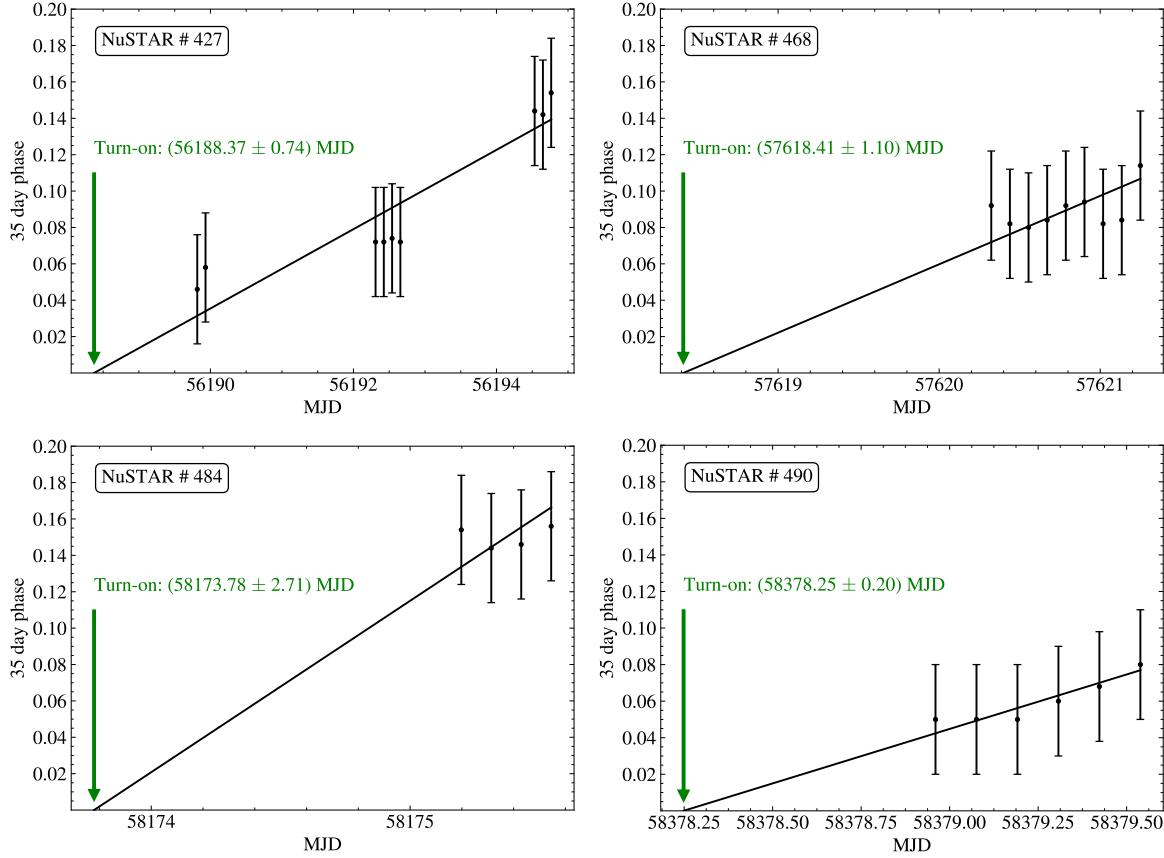


Figure 4.18: Determination of the phase zero/turn-on time based on pulse profile fitting (O^{PP}) on the basis of *NuSTAR* data using a free parameter for the slope.

Table 4.7: Inferred cycle lengths from the *NuSTAR* and *HXMT* data by using a linear regression where the slope is kept as a free parameter. The cycle length then corresponds to the inverse of the slope.

<i>NuSTAR</i>		<i>HXMT</i>	
Cycle no.	Cycle length [d]	Cycle no.	Cycle length [d]
427	45.88 ± 7.36	477	13.12 ± 5.93
457	*	478	**
468	26.59 ± 12.27	483	148.68 ± 92.38
478	**	484	*
484	10.62 ± 18.18	486	23.44 ± 11.03
490	16.78 ± 3.33	487	38.43 ± 10.86
494	*	489	28.92 ± 13.91
495	*	494	47.99 ± 15.96
		495	28.68 ± 4.16

* Not enough points for a fit ** See discussion in text

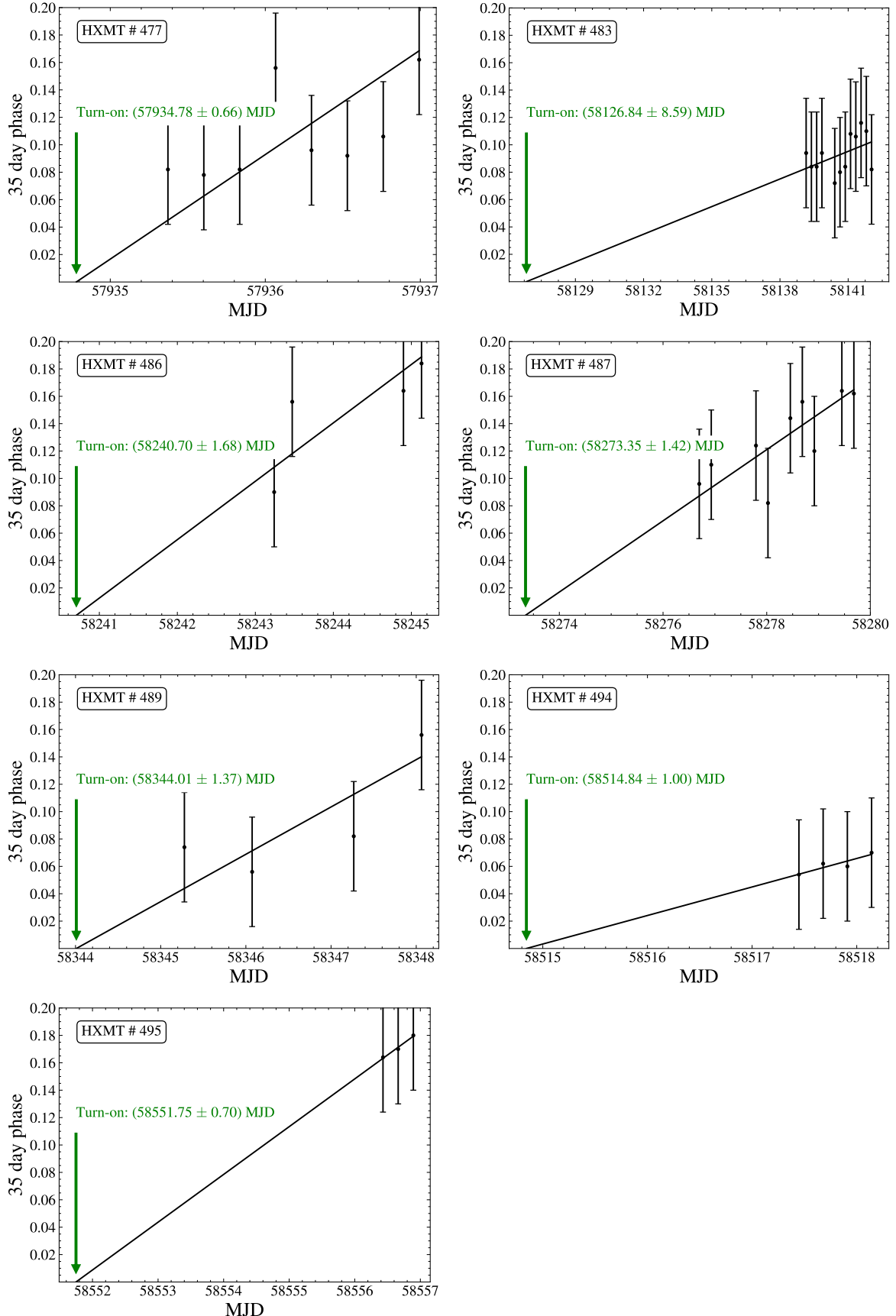


Figure 4.19: Determination of the phase zero/turn-on time based on pulse profile fitting (O^{PP}) on the basis of *HXMT* data using a free parameter for the slope.

Table 4.8: Summary of the *NuSTAR* observations of the phase zero values calculated (C) and determined using the observed turn-on based on the light curve (O^{LC}) and with pulse profile fitting (O^{PP}). The ($O-C$) data can be seen in the last two columns, respectively.

Cycle no.	C [MJD]	O^{LC} [MJD]	O^{PP} [MJD]	$(O^{LC}-C)$ [days]	$(O^{PP}-C)$ [days]
427	56177.05	56189.00 \pm 0.10	56188.37 \pm 0.74	11.95	11.06
457	57222.66	57233.50 \pm 0.10	*	10.84	*
468	57606.04	57617.22 \pm 0.12	57618.41 \pm 1.10	11.18	12.00
478	57954.58	57965.70 \pm 0.20	**	11.14	**
484	58163.70	58171.50 \pm 0.50	58173.78 \pm 2.71	7.80	10.12
490	58372.82	58377.67 \pm 0.30	58378.25 \pm 0.20	4.85	5.42
494	58512.23	58516.57 \pm 0.20	*	4.34	*
495	58547.09	58551.50 \pm 0.70	*	4.41	*

* Not enough points for a fit ** See discussion in text

Table 4.9: Summary of the *HXMT* observations of the phase zero values calculated (C) and determined using the observed turn-on based on the light curve (O^{LC}) and with pulse profile fitting (O^{PP}). The ($O-C$) data can be seen in the last two columns, respectively.

Cycle no.	C [MJD]	O^{LC} [MJD]	O^{PP} [MJD]	$(O^{LC}-C)$ [days]	$(O^{PP}-C)$ [days]
477	57919.72	57931.55 \pm 0.30	57934.78 \pm 0.66	11.83	15.05
478	57954.58	57965.70 \pm 0.20	**	11.12	**
483	58128.84	58136.60 \pm 0.20	58126.84 \pm 8.59	7.76	-2.00
484	58163.70	58171.50 \pm 0.50	*	7.80	*
486	58233.40	58239.23 \pm 0.06	58240.70 \pm 1.68	5.83	7.30
487	58268.26	58274.08 \pm 0.08	58273.35 \pm 1.42	5.82	5.09
489	58337.97	58342.82 \pm 0.10	58344.01 \pm 1.37	4.85	6.04
494	58512.23	58516.57 \pm 0.20	58514.84 \pm 1.00	4.34	2.61
495	58547.09	58551.50 \pm 0.70	58551.75 \pm 0.70	4.66	4.41

* Not enough points for a fit ** See discussion in text

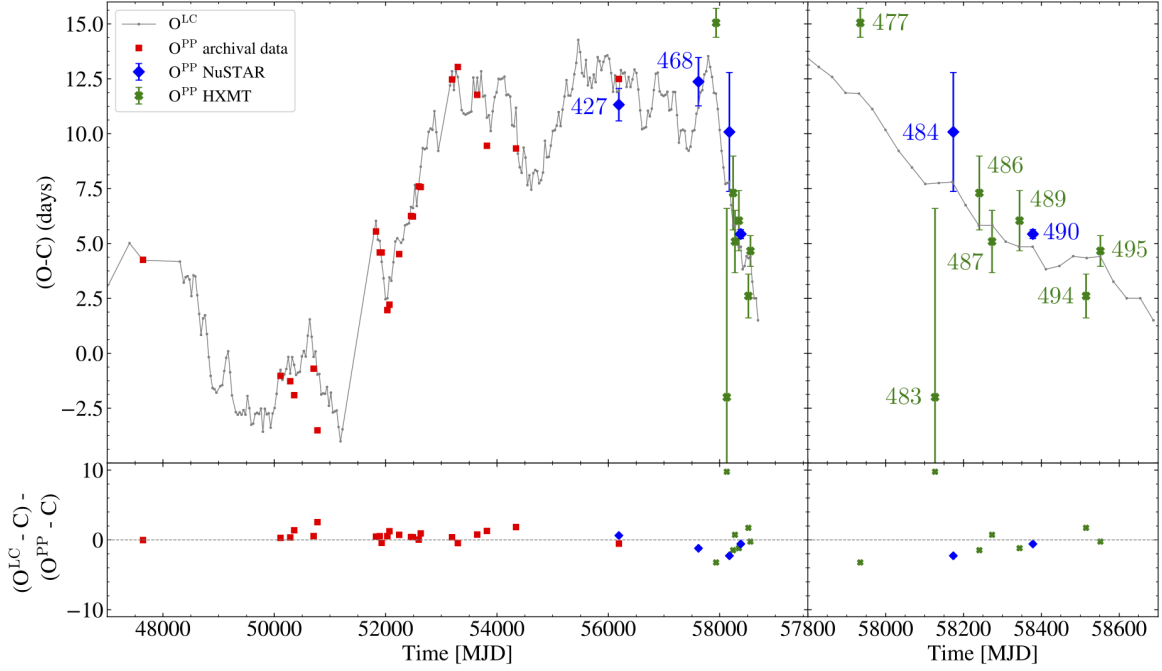


Figure 4.20: Updated (O-C) diagram. The (O^{LC} -C) data is shown in gray, the (O^{PP} -C) data from Staubert et al. (2013) is displayed in red squares, the *NuSTAR* data in blue diamonds and the *HXMT* as green crosses. The right panel shows a zoom-in to the last 800 days and the bottom panels shows the residuals.

The results can be summarized as follows:

- From the *NuSTAR* data, cycles 427, 468 and 490 track the observed turn-ons quite well. Cycle 484 shows a turn-on later than observed, but within the error bounds.
- For the *HXMT* observations, cycles 486, 487, 489, 494 and 495 track the (O-C) evolution very well, while cycles 477 and 483 imply a turn on that happens later and sooner than the observed turn-on, respectively.

B: Best fit using combined data. On the basis of the assumption that there is a long term trend in the evolution of the pulse profiles, which might not be seen on short time scales or with few points, the data was fit together (all cycles of *NuSTAR* and *HXMT*) to determine a best fitting slope and therefore an inferred cycle length. The y-intercept was independent for all cycles. Using this approach, a best fit was achieved for a cycle length of (54.08 ± 8.04) d, which is inconsistent at greater than two sigma confidence interval with the expected super-orbital cycle length of 34.85 d.

For comparison, the χ^2 values were calculated for both cases, yielding:

$$\begin{aligned} 34.85 \text{ d} : \quad & \chi^2 = 176.66 \text{ (75 dof)}, \\ 54.08 \text{ d} : \quad & \chi^2 = 161.88 \text{ (74 dof)}, \end{aligned}$$

indicating that the cycle length of about 54 d results in a better fit. Since the χ^2 values are very close, however, this suggests that the pulse profiles might not change as regularly with super-orbital phase as previously assumed. When calculating the

p-value to measure the goodness of the fits, they are 1.04×10^{-10} and 4.68×10^{-9} for a 34.85 d and 54.08 d cycle length, respectively. Since these values are very small, the data does not appear to be consistent with the hypothesized distribution in either case. Also noteworthy is that the best fitting result is in first approximation about

$$54 \text{ d} \approx \frac{3}{2} \times 35 \text{ d},$$

which might indicate that this is produced by how the data is sampled and a solution of 35 d can not be discarded as a possible result. The results from these tests are not conclusive: it is physically not reasonable to assume that the super-orbital cycle length is 54 d long but neither can the model of a 35 d cycle be confirmed or rejected based on the data.

C: Phase LC vs. Phase PP. In order to investigate this finding further, the super-orbital phases based on the light curves (ϕ^{LC}) and based on pulse profile fitting (ϕ^{PP}) were compared and their distributions analyzed. In the following, it is assumed that the calculated phases based on the light curve data are the “correct” phases. In Figure 4.21, ϕ^{PP} is plotted over ϕ^{LC} with their corresponding uncertainties. The diagonal line is the axis bisector and in the ideal case, all points would fall along this line. If this were the case, then the same phases would be determined using both methods.

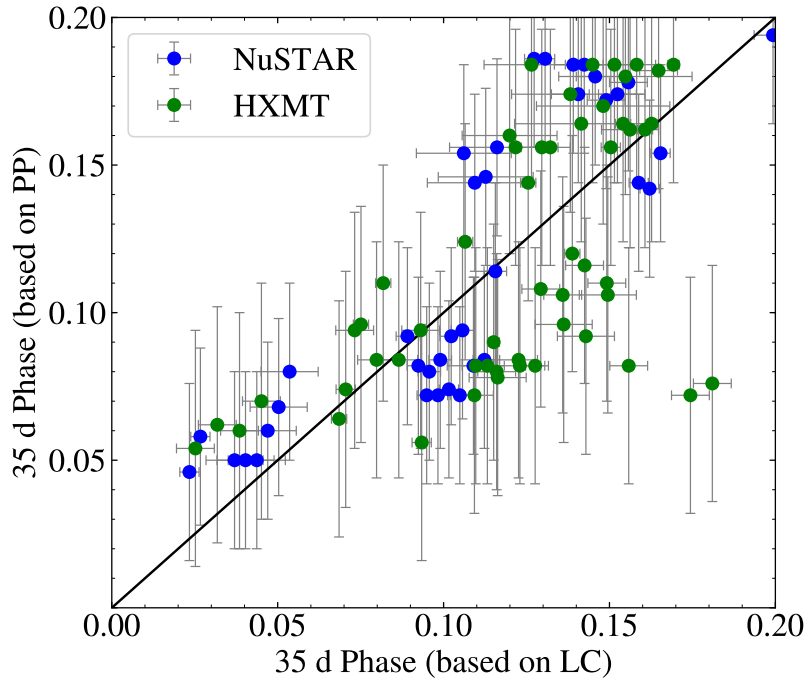


Figure 4.21: ϕ^{PP} vs. ϕ^{LC} plot including the respective uncertainties. The diagonal line is the axis bisector and serves to guide the eye.

Since the uncertainties, especially those of ϕ^{PP} , are very large, they have been removed in Figure 4.22 for a better overview. Also, the different cycles have been color coded and the top and right panels of the Figure show the histograms of the respective data.

Several things can be seen in this Figure:

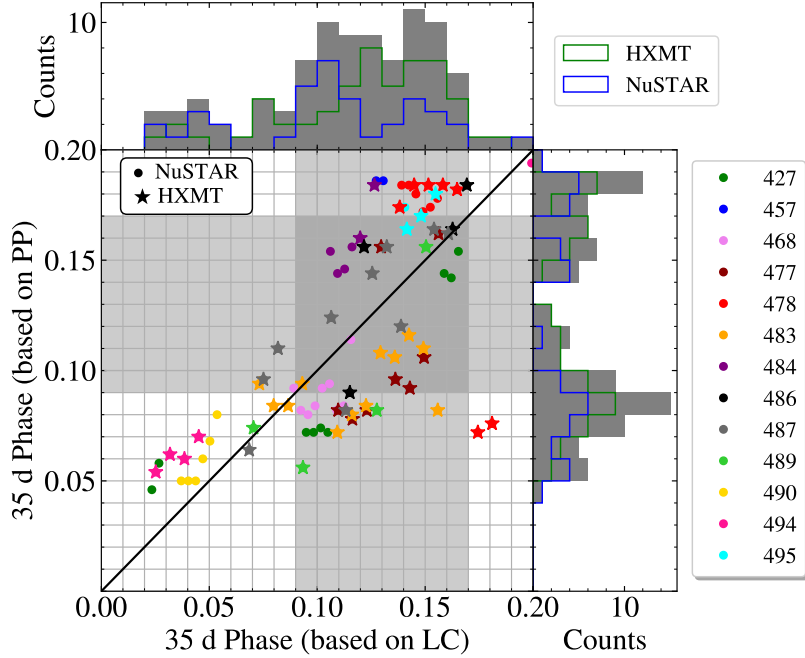


Figure 4.22: ϕ^{PP} vs. ϕ^{LC} plot including histograms of each. The cycles are color coded and the combined histograms of *HXMT* (green outline) and *NuSTAR* (blue outline) data is shaded in dark gray in the top and right panels. The ϕ^{LC} range including the majority of the points (69, between phase 0.09 and 0.17) is shaded in light gray on both axes.

- Above a phase of 0.09 of ϕ^{LC} and 0.07 of ϕ^{PP} , a high scatter of the points can be seen;
- the majority of the points (69 in total) of ϕ^{LC} - the “correct” phases - are located between phases of 0.09 and 0.17 as can be seen in the combined histogram (in the top panel shaded in gray), which is highlighted in light gray in the main figure. The same phase range of the ϕ^{PP} , also shaded in light gray shows a very different distribution and only 36 points have been determined in this range;
- cycle 478 is especially interesting: All except for two points have been determined in a ϕ^{LC} range between 0.13 and 0.18 whereas ϕ^{PP} results in a range between 0.17 and 0.19;
- the distribution of ϕ^{PP} , shown in the right panel, appears to be bimodal around 0.085 and 0.17, whereas no observations were found to have a phase around 0.135 with the pulse profile fitting method.

The different distributions in the data make especially clear that the different methods of determining the 35 d phase do not yield the same results and therefore cannot be regarded as equivalent. The *NuSTAR* and *HXMT* pulse profiles tend to not fit a significant fraction of the *RXTE* pulse profile template ($0.09 < \phi < 0.17$) well enough, which leads to an incorrect calculation of the turn-on times.

4.3.5 Pulsed Fraction

The pulsed fraction depends on many factors such as the configuration of the X-ray emitting regions, the dipole position relative to the observer and the energy (Lutovinov & Tsygankov 2009). There are different ways to define the pulsed fraction, such as

$$\text{PF}^{\text{minmax}} = \frac{I_{\text{max}} - I_{\text{min}}}{I_{\text{max}} + I_{\text{min}}} \quad (4.3)$$

$$\text{PF}^{\text{area}} = \frac{I^{\text{Pulse}}}{I^{\text{Pulse}} + I^{\text{DC}}} \quad (4.4)$$

where I^{Pulse} and I^{DC} ⁶ are defined as

$$I^{\text{Pulse}} = \int_0^1 (I(\phi) - I_{\text{min}}) d\phi \approx \sum_0^{n=128} (I_n - I_{\text{min}})$$

$$I^{\text{DC}} = \int_0^1 I_{\text{min}} d\phi \approx \sum_0^{n=128} I_{\text{min}} = 128 \times I_{\text{min}}$$

with n the number of phase bins (in our case 128), I_n are the counts in the n th phase bin and I_{min} , I_{max} are the minimum and maximum counts measured, respectively. The different components are also illustrated in Figure 4.23.

In the following, the pulsed fraction of Her X-1 will be investigated based on the *NuSTAR* observations. In Figure 4.24, energy-phase matrices are shown with the pulsed fraction color coded. Figure 4.24a shows the results for PF^{area} and 4.24b for $\text{PF}^{\text{minmax}}$. In both matrices, a clear dip in the pulsed fraction can be seen between 2 to 8 keV. Another feature can be observed between 30 to 45 keV, which is more pronounced in the $\text{PF}^{\text{minmax}}$ plot. Also, the pulsed fraction appears to decrease with 35 d phase and the latter feature can only be made out in phases greater than about 0.1.

For a better analysis, $\text{PF}^{\text{minmax}}$ and PF^{area} are shown for the combined observations in the energy range 1 to 58 keV at 1 keV resolution in Figure 4.25. As expected, for both definitions of the pulsed fraction, a dip in pulsed fraction can be seen between 2 to 8 keV. This feature is caused by the iron K α line, which is also indicated in the figure at 6.4 keV. The observed shift to lower energies could be due to a poor resolution.

Her X-1 is also known to have a cyclotron line around 37 keV (Staubert et al. 2019), which can also be seen in the Figure. In PF^{area} , the line appears to be more pronounced, while in the $\text{PF}^{\text{minmax}}$ calculation, it seems to be noisier.

Also observed is the hint of an unknown feature around 48 keV. Further analysis is needed to understand if this is an actual feature or just due to statistical fluctuations or other instrumental influences.

Overall, the pulsed fraction is increasing with increasing energy. This has been observed before, for example by Lutovinov & Tsygankov (2009); Klochkov et al. (2008) (see also Figure 2.10). As can be expected from the definitions in Equations 4.4 and 4.3, $\text{PF}^{\text{minmax}}$ overestimates the pulsed fraction and PF^{area} yields more accurate results. A more detailed discussion of the different estimators for the pulsed fraction can be found in An et al. (2015).

⁶In this context, DC refers to the constant count value that is detected in all channels.

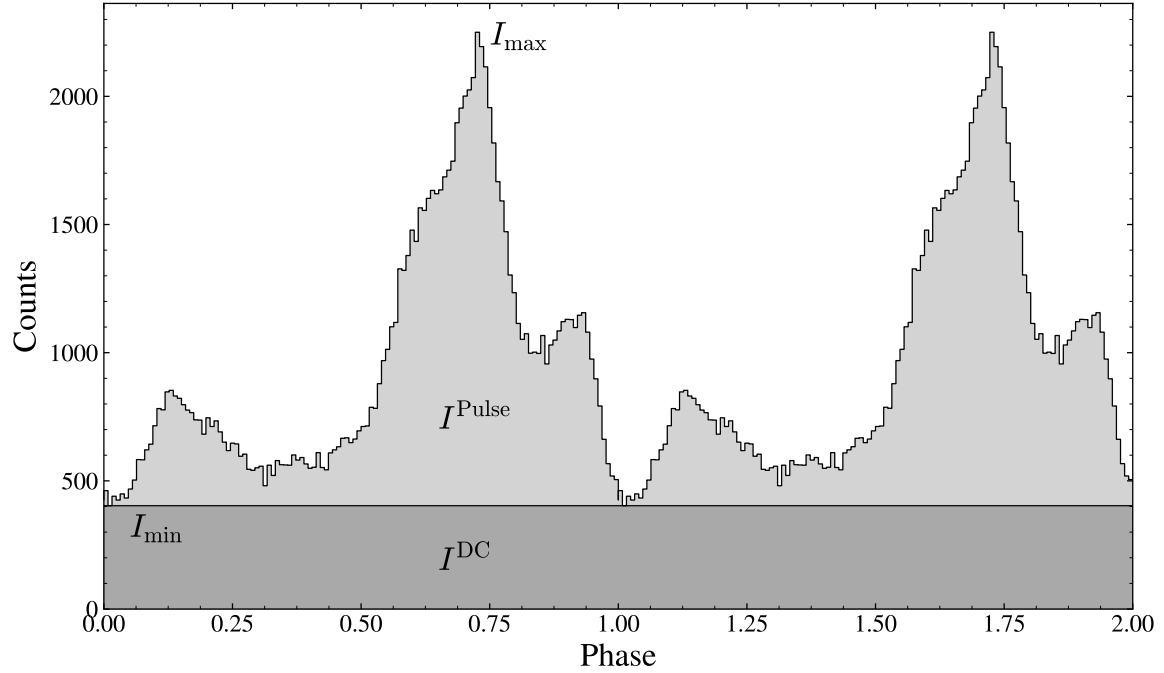


Figure 4.23: Definition of the various elements to determine the pulsed fractions $\text{PF}^{\text{minmax}}$ and PF^{area} : I_{min} and I_{max} are the minimum and maximum counts measured, I^{DC} describes the area below a constant I_{min} , shaded in dark gray and I^{Pulse} describes the area between the detected counts and the DC value, shaded in light gray. The example shows *NuSTAR* observation 10202002002 at an energy range of 9 to 13 keV, which is a typical X-ray pulse profile of Her X-1 during a main-on state.

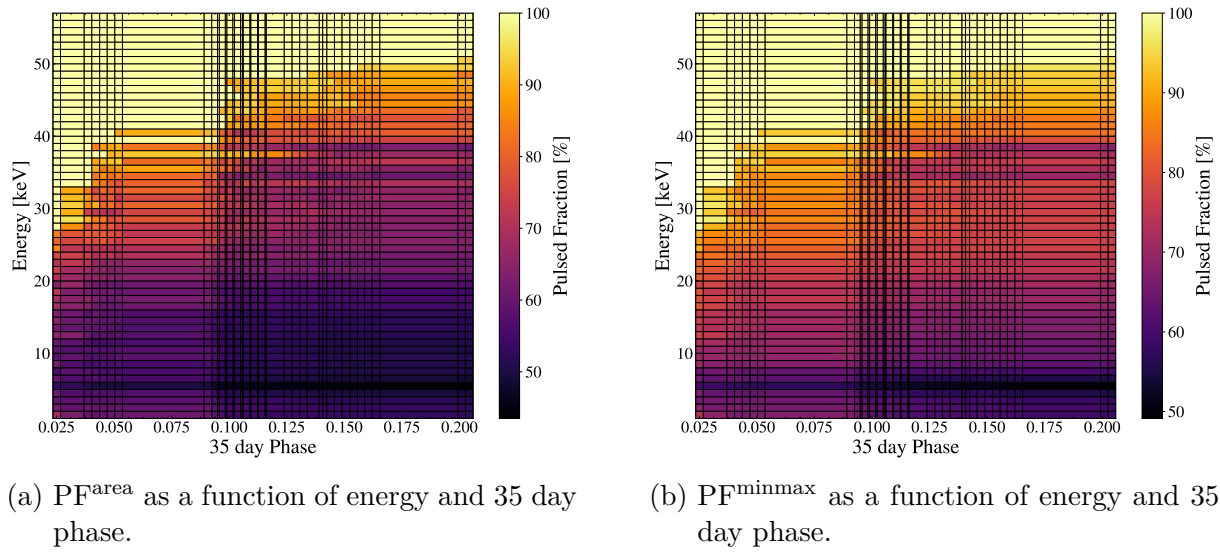


Figure 4.24: Pulsed fraction as a function of energy and 35 day phase. Figure (a) shows the PF^{area} definition and (b) $\text{PF}^{\text{minmax}}$.

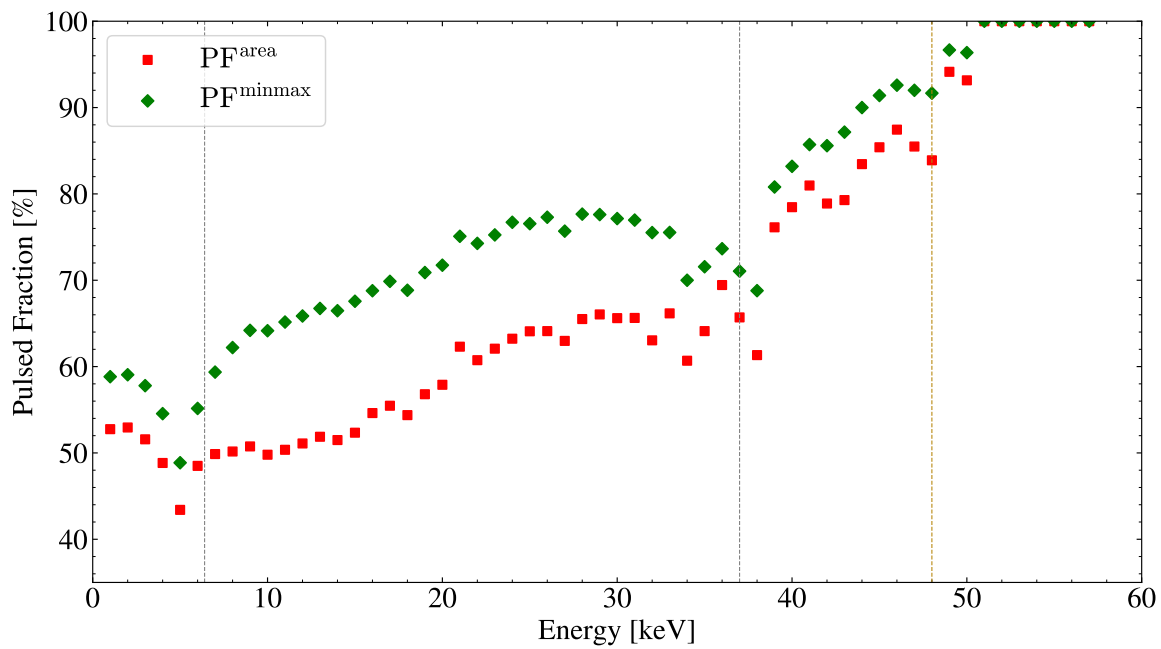


Figure 4.25: Pulsed fraction as a function of energy of the combined *NuSTAR* observations. The vertical gray dashed lines indicate the centroid of the iron K α line and the cyclotron line at 6.4 keV and 37 keV, respectively. The yellow dashed line indicates the energy of an unknown observed feature in the pulsed fraction at 48 keV.

Discussion & Conclusions

In this thesis, the X-ray binary pulsar Her X-1 was studied using data from the observatories *NuSTAR* and *HXMT*. First, energy-phase matrices were created for all observations, divided into 10 000 s (*NuSTAR*) and 20 000 s (*HXMT*) intervals. While most matrices showed the expected two-peaked structure including a main pulse and a fainter interpulse, some matrices already hinted at a new feature as some observations showed four instead of two pulses. These features could be better observed by creating pulse profiles in several energy ranges. Most profiles showed the expected pre-interpulse minimum, followed by the interpulse and a main pulse with a trailing and leading shoulder and a sharp edge that has been presented in many publications (Deeter et al. 1998; Klochkov et al. 2008; Staubert et al. 2013).

The observations of cycles 457, 478, 484 and 495, however, showed the new features that were already indicated in the matrices, also referred to as the “four-peaked” structure. The pulse profiles appear to show additional peaks, especially in low energy ranges below 13 keV. The interpulse and main pulse are still present, but more pronounced than in the “normal” profiles and a new peak appears between the interpulse and the main pulse. This could possibly be an evolution of the left shoulder, becoming more independent. The right shoulder also becomes more pronounced and appears as a second main pulse to the right of the original. The cause of these new features is unknown and it appears to be variable, as multiple profiles have been observed in-between these pulse profiles, which did not show the “four-peaked” structure.

Three cycles in which the “four-peaked” structure has been observed were observed by both *NuSTAR* and *HXMT* and a direct comparison shows the same basic features. This leads to the conclusion that the new structure is not caused by the instruments but due to an actual physical change in the system. A four peaked structure could be caused, for example, by a magnetic quadrupole field.

Based on the pulse profiles in the 9 keV to 13 keV energy range, the super-orbital phase was then determined using the pulse profile fitting method and a pulse profile template based on *RXTE* data. The newly observed four peaked structure, however, suggests that a new template might be needed to include these features and ensure a correct fit. This requires extended observations that are not yet available. Therefore, the current *RXTE* pulse profile template was used to determine the super-orbital phase, and subsequently the zero phase/turn-on time of the cycle was calculated. To do this, a model was used assuming that the super-orbital phase lasts 34.85 d. The corresponding (O-C) diagram was created and the data from the pulse profiles tracks the results based on the light curve data very well.

The pulse profile fitting method was deemed to be in need of further testing after an examination of the results of the turn-on time determination, starting with an assessment of the assumptions made. Since the method was initially used to investigate if the system contains “two-clocks” or indeed only one “clock”, the independence of the method using a fixed cycle length of 34.85 d remains open to question. It is unclear

if the pulse profiles evolve systematically and regularly enough with the super-orbital period to infer from the observations alone on the turn-on time of the cycles. To test this, first a linear regression was used instead of an extrapolation to determine the cycle length of each cycle. The results varied largely and it should be emphasized that this is not believed to be due to physical changes in the system, as it is unreasonable to assume that the super-orbital cycle lengths vary by large factors within a few cycles. However, these results do seem to indicate a possible shortcoming in the method as the data do not show the 34.85 d cycle length that is generally assumed.

The results for the linear regression also allowed for the determination of a turn-on time and the corresponding (O-C) diagram was created. The results with this method also appear to track the observed turn-on times based on the light curve data mostly well, but with much larger uncertainties. This leads to the tentatively confirmed conclusion that only one “clock” is present in the system, as previously shown by Staubert et al. (2013).

Since it is possible that by fitting the individual cycles a more long-term trend is overlooked, the data of *NuSTAR* and *HXMT* was combined and the best fit was determined for a cycle length of about 54 d. This serves as another indication that the pulse profile fitting method can possibly not be used for its intended purposes. It is again emphasized though that this result is not believed to be physically correct, but only shows that the method itself might have shortcomings.

The last aspect that was investigated to test the method was the ϕ^{PP} vs ϕ^{LC} plot, which showed a large scatter and raised more concerns about the accuracy of the determined phases from pulse profile fitting. Most phases that were determined from the observed turn-on from the light curve were not correctly identified with the pulse profile fitting method. The distributions of the respective phases also revealed large differences and the distribution of the phases based on pulse profile fitting appears to be bimodal.

In a last part of the work, the pulsed fraction was calculated for the *NuSTAR* data. Overall, the pulsed fraction increased with increasing energy, which confirms previous findings. This increase is commonly attributed to geometric effects. Softer photons are generally expected to be emitted at the upper part of the accretion column and therefore they can be seen during a larger part of the NS spin. Harder photons, on the other hand, are generally emitted closer to the NS surface and therefore they are screened by the NS surface itself for most of the spin period. Additionally, the iron K α line was identified in the energy dependent pulsed fraction, as well as the cyclotron line at around 37 keV.

35 d Phases

Table 1: Results for the 35 d phases of the *NuSTAR* data. Each observation is split in 10 000 s intervals, indicated by the “No” of observation. Also shown is the cycle and the center time of observations T_0 [MJD]. In the last two columns, the 35 d phases are shown, first based on the observed turn-on based on light curve data (ϕ^{LC}) and second based on the pulse profile (ϕ^{PP}) fitting. For a better overview, results with 35 d phase > 0.2 are not listed, as they are discarded in the further analysis.

Observation ID	No	Cycle	T_0 [MJD]	ϕ^{LC}	ϕ^{PP}
30002006002	1	427	56189.8158028	0.023 ± 0.003	0.046 ± 0.03
30002006002	2	427	56189.9315435	0.027 ± 0.003	0.058 ± 0.03
30002006005	1	427	56192.3089403	0.095 ± 0.003	0.072 ± 0.03
30002006005	2	427	56192.4246810	0.098 ± 0.003	0.072 ± 0.03
30002006005	3	427	56192.5404218	0.102 ± 0.003	0.074 ± 0.03
30002006005	4	427	56192.6561625	0.105 ± 0.003	0.072 ± 0.03
30002006007	1	427	56194.5334770	0.159 ± 0.003	0.144 ± 0.03
30002006007	2	427	56194.6492178	0.162 ± 0.003	0.142 ± 0.03
30002006007	3	427	56194.7649585	0.165 ± 0.003	0.154 ± 0.03
90102002002	2	457	57237.9349791	0.127 ± 0.003	0.186 ± 0.03
90102002002	3	457	57238.0507199	0.131 ± 0.003	0.186 ± 0.03
10202002002	1	468	57620.3234952	0.089 ± 0.003	0.092 ± 0.03
10202002002	2	468	57620.4392359	0.092 ± 0.003	0.082 ± 0.03
10202002002	3	468	57620.5549766	0.096 ± 0.003	0.080 ± 0.03
10202002002	4	468	57620.6707174	0.099 ± 0.003	0.084 ± 0.03
10202002002	5	468	57620.7864581	0.102 ± 0.003	0.092 ± 0.03
10202002002	6	468	57620.9021989	0.106 ± 0.003	0.094 ± 0.03
10202002002	7	468	57621.0179396	0.109 ± 0.003	0.082 ± 0.03
10202002002	8	468	57621.1336803	0.112 ± 0.003	0.084 ± 0.03
10202002002	9	468	57621.2494211	0.116 ± 0.003	0.114 ± 0.03
30302012002	1	478	57970.5467838	0.139 ± 0.006	0.184 ± 0.03
30302012002	2	478	57970.6625246	0.142 ± 0.006	0.184 ± 0.03
30302012002	3	478	57970.7782653	0.146 ± 0.006	0.180 ± 0.03
30302012002	4	478	57970.8940060	0.149 ± 0.006	0.172 ± 0.03
30302012002	5	478	57971.0097468	0.152 ± 0.006	0.174 ± 0.03
30302012002	6	478	57971.1254875	0.156 ± 0.006	0.178 ± 0.03
30302012004	1	484	58175.1978552	0.106 ± 0.014	0.154 ± 0.03
30302012004	2	484	58175.3135959	0.109 ± 0.014	0.144 ± 0.03
30302012004	3	484	58175.4293367	0.113 ± 0.014	0.146 ± 0.03
30302012004	4	484	58175.5450774	0.116 ± 0.014	0.156 ± 0.03

Table 1: (Continued)

Observation ID	No	Cycle	T_0 [MJD]	ϕ^{LC}	ϕ^{PP}
30402009002	1	490	58378.9601051	0.037 ± 0.009	0.050 ± 0.03
30402009002	2	490	58379.0758459	0.040 ± 0.009	0.050 ± 0.03
30402009002	3	490	58379.1915866	0.044 ± 0.009	0.050 ± 0.03
30402009002	4	490	58379.3073274	0.047 ± 0.009	0.060 ± 0.03
30402009002	5	490	58379.4230681	0.050 ± 0.009	0.068 ± 0.03
30402009002	6	490	58379.5388088	0.054 ± 0.009	0.080 ± 0.03
30402034002	1	494	58523.5154022	0.199 ± 0.006	0.194 ± 0.03
30402034008	1	495	58556.3994771	0.141 ± 0.020	0.174 ± 0.03

Table 2: Results for the 35 d phases of the *HXMT* data. Each observation is split in 20 000 s intervals, indicated by the “No” of observation. Also shown is the cycle and the center time of observations T_0 [MJD]. In the last two columns, the 35 d phases are shown, first based on the observed turn-on based on light curve data (ϕ^{LC}) and second based on the pulse profile (ϕ^{PP}) fitting. For a better overview, results with 35 d phase > 0.2 are not listed, as they are discarded in the further analysis.

Obs ID P01013080XX	No	Cycle	T_0 [MJD]	ϕ^{LC}	ϕ^{PP}
01	1	477	57935.3719925	0.110 ± 0.009	0.082 ± 0.04
01	2	477	57935.6034740	0.116 ± 0.009	0.078 ± 0.04
01	3	477	57935.8349554	0.123 ± 0.009	0.082 ± 0.04
01	4	477	57936.0664369	0.130 ± 0.009	0.156 ± 0.04
01	5	477	57936.2979184	0.136 ± 0.009	0.096 ± 0.04
01	6	477	57936.5293999	0.143 ± 0.009	0.092 ± 0.04
01	7	477	57936.7608814	0.150 ± 0.009	0.106 ± 0.04
01	8	477	57936.9923629	0.156 ± 0.009	0.162 ± 0.04
02	1	478	57970.5179075	0.138 ± 0.006	0.174 ± 0.04
02	2	478	57970.7493890	0.145 ± 0.006	0.184 ± 0.04
02	3	478	57970.9808704	0.152 ± 0.006	0.184 ± 0.04
02	4	478	57971.2123519	0.158 ± 0.006	0.184 ± 0.04
02	5	478	57971.4438334	0.165 ± 0.006	0.182 ± 0.04
03	1	478	57971.7777455	0.174 ± 0.006	0.072 ± 0.04
03	2	478	57972.0092270	0.181 ± 0.006	0.076 ± 0.04
04	1	483	58139.1511715	0.073 ± 0.006	0.094 ± 0.04
04	2	483	58139.3826530	0.080 ± 0.006	0.084 ± 0.04
04	3	483	58139.6141344	0.087 ± 0.006	0.084 ± 0.04
04	4	483	58139.8456159	0.093 ± 0.006	0.094 ± 0.04
05	1	483	58140.4102685	0.109 ± 0.006	0.072 ± 0.04
05	2	483	58140.6417500	0.116 ± 0.006	0.080 ± 0.04
05	3	483	58140.8732314	0.123 ± 0.006	0.084 ± 0.04
05	4	483	58141.1047129	0.129 ± 0.006	0.108 ± 0.04
05	5	483	58141.3361944	0.136 ± 0.006	0.106 ± 0.04
05	6	483	58141.5676759	0.143 ± 0.006	0.116 ± 0.04

Table 2: (Continued)

Obs ID P01013080XX	No	Cycle	T_0 [MJD]	ϕ^{LC}	ϕ^{PP}
05	7	483	58141.7991574	0.149 ± 0.006	0.110 ± 0.04
05	8	483	58142.0306389	0.156 ± 0.006	0.082 ± 0.04
06	1	484	58175.6773635	0.120 ± 0.014	0.160 ± 0.04
06	2	484	58175.9088450	0.127 ± 0.014	0.184 ± 0.04
07	1	486	58243.2413565	0.115 ± 0.002	0.090 ± 0.04
07	2	486	58243.4728380	0.122 ± 0.002	0.156 ± 0.04
08	1	486	58244.8990415	0.164 ± 0.002	0.164 ± 0.04
08	2	486	58245.1305230	0.169 ± 0.002	0.184 ± 0.04
13	2	487	58276.6984510	0.075 ± 0.002	0.096 ± 0.04
13	3	487	58276.9299324	0.082 ± 0.002	0.110 ± 0.04
14	1	487	58277.7922705	0.107 ± 0.002	0.124 ± 0.04
14	2	487	58278.0237520	0.113 ± 0.002	0.082 ± 0.04
15	1	487	58278.4548975	0.126 ± 0.002	0.144 ± 0.04
15	2	487	58278.6863790	0.132 ± 0.002	0.156 ± 0.04
15	3	487	58278.9178604	0.139 ± 0.002	0.120 ± 0.04
16	1	487	58279.4488335	0.154 ± 0.002	0.164 ± 0.04
16	2	487	58279.6803150	0.161 ± 0.002	0.162 ± 0.04
17	1	489	58345.2782195	0.071 ± 0.003	0.074 ± 0.04
18	1	489	58346.0735665	0.093 ± 0.003	0.056 ± 0.04
19	1	489	58347.2666685	0.128 ± 0.003	0.082 ± 0.04
20	1	489	58348.0621205	0.150 ± 0.003	0.156 ± 0.04
22	1	494	58517.4473405	0.025 ± 0.006	0.054 ± 0.04
22	2	494	58517.6788220	0.032 ± 0.006	0.062 ± 0.04
22	3	494	58517.9103034	0.039 ± 0.006	0.060 ± 0.04
22	4	494	58518.1417849	0.045 ± 0.005	0.070 ± 0.04
26	1	495	58556.4304535	0.142 ± 0.020	0.164 ± 0.04
26	2	495	58556.6619350	0.148 ± 0.020	0.170 ± 0.04
26	3	495	58556.8934164	0.155 ± 0.020	0.180 ± 0.04

Bibliography

- An, H., Archibald, R. F., Hascoët, R., et al. 2015, ApJ, 807, 93
- Arnaud, K., Smith, R., & Siemiginowska, A. 2011, Handbook of X-ray Astronomy
- Basko, M. M. & Sunyaev, R. A. 1976, MNRAS, 175, 395
- Buccheri, R., Bennett, K., Bignami, G. F., et al. 1983, A&A, 128, 245
- Courvoisier, T. J.-L. 2013, High Energy Astrophysics
- Deeter, J. E., Scott, D. M., Boynton, P. E., et al. 1998, ApJ, 502, 802
- Forster, K., Grefenstette, B., & Madsen, K. 2014, NuSTAR Data Analysis Quickstart Guide
- Harrison, F. A., Craig, W. W., Christensen, F. E., et al. 2013, ApJ, 770, 103
- Huppenkothen, D., Bachetti, M., Stevens, A., et al. 2019, The Journal of Open Source Software, 4, 1393
- Jones, C. & Forman, W. 1976, ApJL, 209, L131
- Klochkov, D., Staubert, R., Postnov, K., et al. 2008, A&A, 482, 907
- Leahy, D. A. & Abdallah, M. H. 2014, ApJ, 793, 79
- Lipunov, V. M. 1987, Astrophysics of neutron stars
- Longair, M. S. 2011, High Energy Astrophysics
- Lutovinov, A. A. & Tsygankov, S. S. 2009, Astronomy Letters, 35, 433
- Meszaros, P. 1984, SSR, 38, 325
- Perri, M., Puccetti, S., Spagnuolo, N., et al. 2017, The NuSTAR Data Analysis Software Guide
- Reynolds, A. P., Quaintrell, H., Still, M. D., et al. 1997, MNRAS, 288, 43
- Scott, D. M., Leahy, D. A., & Wilson, R. B. 2000, ApJ, 539, 392
- Shapiro, S. L. & Teukolsky, S. A. 1983, Black holes, white dwarfs, and neutron stars: The physics of compact objects
- Staubert, R., Bezler, M., & Kendziorra, E. 1983, A&A, 117, 215
- Staubert, R., Klochkov, D., Fürst, F., et al. 2017, A&A, 606, L13
- Staubert, R., Klochkov, D., Postnov, K., et al. 2009a, A&A, 494, 1025
- Staubert, R., Klochkov, D., Postnov, K., et al. 2010a, X-ray Astronomy 2009; Present Status, Multi-Wavelength Approach and Future Perspectives, 1248, 209
- Staubert, R., Klochkov, D., Vasco, D., et al. 2013, A&A, 550, A110
- Staubert, R., Klochkov, D., Vasco, D., & Wilms, J. 2010b, in Eighth Integral Workshop. The Restless Gamma-ray Universe (INTEGRAL 2010), 48
- Staubert, R., Klochkov, D., Vasco, D., & Wilms, J. 2010c, in Eighth Integral Workshop. The Restless Gamma-ray Universe (INTEGRAL 2010), 141
- Staubert, R., Klochkov, D., & Wilms, J. 2009b, A&A, 500, 883
- Staubert, R., Trümper, J., Kendziorra, E., et al. 2019, A&A, 622, A61
- Tananbaum, H., Gursky, H., Kellogg, E. M., et al. 1972, ApJL, 174, L143
- Zel'dovich, Y. B. & Shakura, N. I. 1969, Soviet Ast., 13, 175
- Zhang, Y., Ge, M., Song, L., et al. 2019, ApJ, 879, 61

Acknowledgements

The present master thesis would not have been possible without several individuals. I would like to extend my thanks to the following people.

First, I thank Prof. Dott. Andrea Santangelo for his guidance throughout my physics studies. His enthusiasm for science has encouraged me time and again to keep pursuing astrophysics. I would like to thank him for continuing to welcome me in his group and for offering the topic and supervisors for this thesis, as well as for his guidance during the authoring.

Next, I want to thank Dr. Lorenzo Ducci, who supervised the thesis from start to finish. His skill and support accompanied the process at every step and I want to thank him for both his many suggestions as well as the freedom he granted me in the work.

I was lucky to also have Prof. Dr. Rüdiger Staubert as a supervisor to this work and I want to thank him for the guidance, for sharing his extended knowledge on this extraordinary source and for his patience in answering all of my questions.

I would also like to thank Dr. Long Ji for retrieving the *HXMT* data and making it available to me, as well as helping with the data reduction process and providing scripts and many ideas on the way to the completion of the thesis.

I want to thank my office mates for creating an encouraging and fun working atmosphere, for always listening and helping along the way. This thanks can be extended to all the members of the IAAT, who make working on a thesis like this an adventure and great fun.

I thank my friends for their continued support and motivation and my greatest thanks goes to my family who support me unconditionally and endlessly.